

Topics in Cosmology and Quantum Mechanics: Entanglement Harvesting and
Cosmic Bubble Collisions

Andrew Brainerd

Submitted in partial fulfillment of the
requirements for the degree of
Doctor of Philosophy
in the Graduate School of Arts and Sciences

COLUMBIA UNIVERSITY

2017

© 2017
Andrew Brainerd
All rights reserved

ABSTRACT

Topics in Cosmology and Quantum Mechanics: Entanglement Harvesting and
Cosmic Bubble Collisions

Andrew Brainerd

This dissertation explores two topics located in the intersection of quantum mechanics and cosmology. Entanglement harvesting is a phenomenon in which quantum entanglement can develop between the states of two Unruh-DeWitt detectors travelling through spacetime by way of mutual interaction with a scalar quantum field. I numerically explore entanglement harvesting of Unruh-DeWitt detectors in Minkowski space travelling with constant acceleration, generalizing previous analytical results which held only in a limiting case. Cosmic bubble collisions arise in inflationary cosmology as a mechanism to begin reheating at the end of inflation. I extend the previously proposed theory of boom and bust inflation which relies on the existence of a large extra dimension by exploring particular inflationary models in which reheating need not begin the first time that two bubble walls collide. This allows for a smaller lower bound on the size of the compact extra dimension in the boom and bust proposal.

Contents

List of Figures	iii
List of Tables	ix
Acknowledgements	x
Introduction	1
1 Theory of Entanglement and Unruh-DeWitt Detectors	4
1.1 Quantum Entanglement	5
1.2 Unruh-DeWitt Detectors	8
1.3 Entanglement Harvesting	11
1.4 Gauss-Kronrod Quadrature	13
2 Numerical Evaluation of Acceleration-Assisted Entanglement Har-	
vesting	17
2.1 Introduction to the Problem	17
2.2 Basic Set-Up of Detectors	18
2.3 Numerical Evaluation	26

2.4	Discussion	28
3	Background about Cosmic Bubble Collisions and Inflation	34
3.1	Cosmological Inflation	35
3.2	Nucleation and Collision of Cosmic Bubbles	38
3.3	Compact Extra Dimensions	41
3.4	Discretization and the Symplectic Partitioned Runge-Kutta Algorithm	42
4	Coherent Bubble Collisions in Boom and Bust Inflation	46
4.1	Introduction	46
4.2	Basic Set-Up	49
4.3	Numerical Evaluation	57
4.4	Discussion	62
	Conclusion	87
	Bibliography	89

List of Figures

2.1	Region of parameter space which support entanglement harvesting which supports entanglement harvesting for $c_3 = 0.5$. The green region is calculated with the stationary phase approximation, while the region defined by blue dots is calculated numerically.	29
2.2	Region of parameter space which support entanglement harvesting which supports entanglement harvesting for $c_3 = 1.5$. The green region is calculated with the stationary phase approximation, while the region defined by blue dots is calculated numerically.	30
2.3	Region of parameter space which support entanglement harvesting which supports entanglement harvesting for $c_3 = 2.5$. The green region is calculated with the stationary phase approximation, while the region defined by blue dots is calculated numerically.	31
2.4	Region of parameter space which support entanglement harvesting which supports entanglement harvesting for $c_3 = 3.5$. The green region is calculated with the stationary phase approximation, while the region defined by blue dots is calculated numerically.	32

2.5	Region of parameter space which support entanglement harvesting which supports entanglement harvesting for $c_3 = 4.5$. The green region is calculated with the stationary phase approximation, while the region defined by blue dots is calculated numerically.	33
4.1	Evolution of the bubble for the first example of the two-minimum potential. The red lines are the potential minima at $\phi \approx \pm 1$, and the blue line is the value $\phi \approx -3$ to which the field is kicked in the free passage approximation.	64
4.2	Radiation formation around inside the bubble near the wall for the first example of the two-minimum potential. The red line is the vacuum field value, and the gray lines correspond to deviations from this value by 1% of the magnitude of the vacuum field value $\phi \approx 1$	65
4.3	Energy distribution in the first example of the two-minimum potential. Blue represents kinetic energy, yellow represents the stretch potential energy $\frac{1}{2} \left(\frac{\partial\phi}{\partial x}\right)^2$, and green represents potential energy due to $V(\phi)$, all normalized so that total energy (red) is 1. The x-axis depicts time.	66
4.4	Evolution of the bubble for the second example of the two-minimum potential. The red lines are the potential minima at $\phi \approx \pm 1$, and the blue line is the value $\phi \approx -3$ to which the field is kicked in the free passage approximation.	67

4.5	Radiation formation around inside the bubble near the wall or the second example of the two-minimum potential. The red line is the vacuum field value, and the gray lines correspond to deviations from this value by 1% of the magnitude of the vacuum field value $\phi \approx 1$	68
4.6	Energy distribution in the second example of the two-minimum potential. Blue represents kinetic energy, yellow represents the stretch potential energy $\frac{1}{2} \left(\frac{\partial \phi}{\partial x} \right)^2$, and green represents potential energy due to $V(\phi)$, all normalized so that total energy (red) is 1. The x-axis depicts time.	69
4.7	Evolution of the bubble for the first example of the three-minimum potential. The red lines are the potential minima at $\phi \approx 0, \pm 1$, and the blue line is the value $\phi \approx 1$ to which the field is kicked in the free passage approximation.	70
4.8	Zooming in on middle vacuum $\phi \approx 0$ near the walls in the bubble interior after the first collision in the first example of the three-minimum potential. The field inside the bubble remains well within the 1% threshold until the second collision.	71
4.9	Zooming in on top vacuum $\phi \approx 1$ near the walls in the collision region after the first collision in the first example of the three-minimum potential. The field in this region develops radiation which exceeds the 1% threshold, but which does not propagate into the bubble interior.	72

4.10	Energy distribution in the first example of the three-minimum potential. Blue represents kinetic energy, yellow represents the stretch potential energy $\frac{1}{2} \left(\frac{\partial\phi}{\partial x}\right)^2$, and green represents potential energy due to $V(\phi)$, all normalized so that total energy (red) is 1. The x-axis depicts time.	73
4.11	Evolution of the bubble for the second example of the three-minimum potential. The red lines are the potential minima at $\phi \approx 0, \pm 1$, and the blue line is the value $\phi \approx 1$ to which the field is kicked in the free passage approximation.	74
4.12	Zooming in on middle vacuum $\phi \approx 0$ near the walls in the bubble interior after the first collision in the second example of the three-minimum potential. The field inside the bubble remain at around 1% threshold until the second collision.	75
4.13	Zooming in on top vacuum $\phi \approx 1$ near the walls in the collision region after the first collision in the second example of the three-minimum potential. The field in this region develops radiation which exceeds the 1% threshold, but which does not propagage into the bubble interior.	76
4.14	Energy distribution in the second example of the three-minimum potential. Blue represents kinetic energy, yellow represents the stretch potential energy $\frac{1}{2} \left(\frac{\partial\phi}{\partial x}\right)^2$, and green represents potential energy due to $V(\phi)$, all normalized so that total energy (red) is 1. The x-axis depicts time.	77

4.15	Evolution of the bubble for the first example of the sine-Gordon potential. The red lines are the potential minima at $\phi \approx 2\pi n$ for integer n , and the blue line is the value $\phi \approx 4\pi$ to which the field is kicked in the free passage approximation after the first collision.	78
4.16	Zooming in on original bubble interior $\phi \approx 2\pi$ near the walls in the bubble interior after the first collision in the first example of the sine-Gordon potential. The field inside the bubble remains well below the 1% threshold until the second collision.	79
4.17	Zooming in on first collision region vacuum value $\phi \approx 4\pi$ after the first collision in the first example of the sine-Gordon potential. The field inside the collision region has radiation of amplitude well below the 1% threshold level.	80
4.18	Zooming in on second collision region vacuum value $\phi \approx 6\pi$ after the second collision in the first example of the sine-Gordon potential. The field inside the collision region has radiation of amplitude well below 1% threshold level.	81
4.19	Energy distribution in the first example of the sine-Gordon potential. Blue represents kinetic energy, yellow represents the stretch potential energy $\frac{1}{2} \left(\frac{\partial\phi}{\partial x}\right)^2$, and green represents potential energy due to $V(\phi)$, all normalized so that total energy (red) is 1. The x-axis depicts time.	82

4.20	Evolution of the bubble for the second example of the sine-Gordon potential. The red lines are the potential minima at $\phi \approx 2\pi n$ for integer n , and the blue line is the value $\phi \approx 4\pi$ to which the field is kicked in the free passage approximation after the first collision.	83
4.21	Zooming in on original bubble interior $\phi \approx 2\pi$ near the walls in the bubble interior after the first collision in the second example of the sine-Gordon potential. The field inside the bubble remains well within the 1% threshold.	84
4.22	Zooming in on first collision region vacuum value $\phi \approx 4\pi$ after the first collision in the second example of the sine-Gordon potential. The field inside the collision region has high frequency oscillations concentrated near the bubble wall, which are likely to be caused by spatial discretization error.	85
4.23	Energy distribution in the first example of the sine-Gordon potential. Blue represents kinetic energy, yellow represents the stretch potential energy $\frac{1}{2} \left(\frac{\partial\phi}{\partial x}\right)^2$, and green represents potential energy due to $V(\phi)$, all normalized so that total energy (red) is 1. The x-axis depicts time.	86

List of Tables

1.1	Evaluation points and weighting coefficients for Gaussian quadrature with 5 points on $[-1,1]$	14
1.2	Evaluation points and weighting coefficients for Gauss-Kronrod quadrature with 11 points on $[-1,1]$	16
3.1	Coefficients b_i and B_i used in the 4th order symplectic partitioned Runge-Kutta method.	44

Acknowledgements

During my time in graduate school, I have had the pleasure of working with a number of wonderful people to whom I owe thanks. I would like to thank my family, especially my mother and grandmother, for their support during this time. I'd also like to thank my adviser, Brian Greene, as well as the other professors and postdocs at Columbia from whom I have learned so much, including Lam Hui, Janna Levin, Norman Christ, Erick Weinberg, Daniel Kabat, and many others. I'd also like to thank the staff in the Physics Department office for their help with the requests I have had of them over the years.

To my family.

Introduction

Since the beginning of the 20th century, humanity has taken massive strides in its understanding of the physics of both the small-scale physics of the quantum world and the very large-scale physics of cosmology. With regard to the former, the discovery of quantum mechanics and later quantum entanglement challenged the idea of locality as it had been understood in classical physics[1][2]. With regard to the latter, the theory of relativity introduced the idea of a non-trivial geometry of spacetime, with further developments in theory and experiment leading to the discovery that the universe began in the Big Bang about 13.8 billion years ago[3].

More recently, physicists have had the opportunity to explore phenomena which lie in the intersection of quantum theory and cosmology. The study of the early Universe draws upon both fields— a satisfactory understanding of the Planck epoch of the Universe’s history requires an understanding of quantum gravity, while even in the later, lower-temperature inflationary epoch the possibility of quantum tunneling of the inflaton field requires us to take quantum phenomena into account as we explore the cosmological physics of exponential expansion driven by the energy of the inflaton field. The theory of inflation [4] [5] has been a source of much interest over the last

few decades as it offers a solution to the so-called horizon, flatness, and monopole problems of cosmology.

Cosmology and quantum mechanics are also linked via the phenomenon of entanglement harvesting. Entanglement harvesting allows for two Unruh-DeWitt detectors which interact with a quantum field on spacetime to become entangled with each other even in cases where the detectors remain spacelike separated from one another during the time period in which they are actively interacting with the mediating field. The possible development of entanglement between the two detectors depends on various physical parameters of the detectors and their worldlines, but has also been shown to depend on the global structure of the spacetime in which the detectors are located. Thus, we see the phenomenon of entanglement harvesting also links quantum mechanics and cosmology.

In this dissertation, I explore both entanglement harvesting and a particular proposal within inflationary cosmology known as boom and bust inflation[6]. I extend previous results on entanglement harvesting for Unruh-DeWitt detectors undergoing constant acceleration in Minkowski space by application of numerical integration to integrals which had previously only been treated analytically in a limiting case. In the process, I determine the dependence of entanglement harvesting on a new ratio of physical parameters, which drops out of the previous analytical approximations, and I show that in an appropriate limit I recover the known results. The boom and bust inflation proposal provides a link between two otherwise unrelated topics—the physics of compact extra dimensions and the question of the mechanism which triggers reheating at the end of inflation. In the boom and bust proposal, a bubble

in the inflaton field nucleates via Coleman-DeLuccia tunneling, then expands until it collides with itself after wrapping around the compact extra dimension. In the original boom and bust proposal, this self-collision immediately triggers reheating as the result of radiation emitted by the collision. I consider models of the inflaton field for which the first self-collision of the inflaton bubble leads to a coherent transition of the collision region to a new vacuum minimum with a minimum of radiation emission. These models allow for a smaller lower bound on the size of the compact extra dimension necessary for the boom and bust proposal to be viable.

Chapter 1 of this dissertation introduces the theory underlying the physical phenomena underlying the phenomenon of entanglement harvesting, as well as a discussion of the Gauss-Kronrod method of numerical integration used to obtain the results. Chapter 2 contains a discussion of the specifics of the model for which I have extended previous results, as well a discussion as the results obtained. Chapter 3 gives background information about inflationary cosmology, compact extra dimensions, cosmic bubble nucleation and collisions, and the lattice discretization and symplectic partitioned Runge-Kutta methods which are used to obtain the results in Chapter 4 via numerical simulation. Chapter 4 contains discussion of my extension to the boom and bust model of inflation in which reheating is triggered only after multiple self-collisions of the bubble walls.

Chapter 1

Entanglement and Unruh-DeWitt

Detectors

The phenomenon of entanglement harvesting connects quantum mechanics and cosmology by relating the development of entanglement between Unruh-DeWitt detectors each coupled to a quantum field to the properties of the worldlines of those detectors and the spacetime in which the detectors are located. I review the definition of quantum entanglement for pure and mixed states, as well as the Peres-Horodecki criterion for determining whether a mixed state is entangled. I then discuss the definition and properties of Unruh-DeWitt detectors, followed by an introduction to entanglement harvesting.

1.1 Quantum Entanglement

One of the most striking differences between classical and quantum physics is that the latter allows for the existence of the phenomenon known as "entanglement."

A quantum state is described by a unit vector¹ $|\psi\rangle$ in a Hilbert space \mathcal{H} with the dynamics underlying the system described by Hermitian operator \hat{H} called the Hamiltonian, so that the time-evolution of the state (in the Schrödinger picture) given by the Schrödinger equation

$$\hat{H} |\psi\rangle = i\hbar \frac{\partial}{\partial t} |\psi\rangle \quad (1.1)$$

Given two quantum systems with states $|\psi_1\rangle \in \mathcal{H}_1$ and $|\psi_2\rangle \in \mathcal{H}_2$ and Hamiltonians \hat{H}_1 and \hat{H}_2 , the state of the combined system is given by $|\psi\rangle = |\psi_1\rangle \otimes |\psi_2\rangle \in \mathcal{H}_t$, where $\mathcal{H}_t = \mathcal{H}_1 \otimes \mathcal{H}_2$ is the tensor product of Hilbert spaces of the two subsystems and the time-evolution occurs according to Hamiltonian $\hat{H}_t = \hat{H}_1 \otimes 1 + 1 \otimes \hat{H}_2$. Thus the tensor product operator is used to combine the state spaces of two physical systems to make the state space of a single combined system, analagous to how in classical mechanics two systems with phase spaces S_1 and S_2 can be joined into a single system with phase space $S = S_1 \times S_2$ given by the Cartesian product of the phase spaces. However, the tensor product and Cartesian product are very different from one another— any $(s_1, s_2) \in S$ can be split into states $s_1 \in S_1$ and $s_2 \in S_2$, yet there are elements of \mathcal{H}_t which are not of the form $|\psi_1\rangle \otimes |\psi_2\rangle$ and so cannot be used to define states on \mathcal{H}_1 and \mathcal{H}_2 .

¹Strictly speaking, a quantum state is a ray in \mathcal{H} , so that $|\psi\rangle \sim e^{i\theta} |\psi\rangle$ for real θ .

The states $|\psi_t\rangle$ which can be factorized this way are called separable, while those which cannot be factorized are called entangled. The unusual properties of entangled states were first noted by Einstein, Podolsky, and Rosen[1], who used the properties of an entangled state of two particles to argue that quantum mechanics cannot be a complete description of reality. This argument was later criticized by J. S. Bell[2], who proved that any complete description of reality (known in the literature as a hidden variable theory) cannot both satisfy locality and also reproduce the predictions of quantum mechanics. Bell derived an inequality, named Bell's inequality, placing constraints on the values of observables of any local hidden variable theory. He then showed that, for certain entangled states, quantum mechanics makes predictions for observables which violate the inequality, establishing the fundamentally non-classical nature of entangled systems. Since Bell's discovery, a great deal of work (e.g. [7] [8] [9]) has been done on analyzing entangled states and their non-classical behavior, including exploration of doing quantum computation[10] with entangled states. For the purposes of this thesis, the most relevant results are those which allow entangled states to be distinguished from separable states.

Detecting Entanglement

Given a state $|\psi_t\rangle$ in a Hilbert space \mathcal{H}_t , it is frequently desirable to know whether the state is entangled. There are many criteria which have been developed in the literature in order to detect entanglement and measure the degree to which a state is entangled, including the Schmidt rank[11], von Neumann entropy[11], and the Peres-

Horodecki[12][13] criterion (also called the negativity criterion). For the purposes of this thesis, I focus on the Peres-Horodecki criterion of entanglement in the case where \mathcal{H}_1 and \mathcal{H}_2 are both of dimension 2, i.e. the case of two entangled qubits.

The Peres-Horodecki criterion is defined in terms of mixed states ρ given by density matrices, rather than pure states. Using mixed states is required because the quantum state of the two detectors in entanglement harvesting is obtained by taking the partial trace over the field degrees of freedom, which generically yields a mixed state. The generalization of separability to mixed states (for finite dimensional Hilbert spaces) is as follows: a mixed state ρ on \mathcal{H}_t is separable if and only if we can write

$$\rho = \sum_k p_k \rho_k^{(1)} \otimes \rho_k^{(2)} \quad (1.2)$$

for $\{\rho_k^{(1)}\}$ and $\{\rho_k^{(2)}\}$ finite families of mixed states on \mathcal{H}_1 and \mathcal{H}_2 and $\{p_k\}$ a probability distribution, i.e. $p_k \geq 0$ and $\sum p_k = 1$. In other words, ρ must be a *classical* probabilistic mixture of mixed states on \mathcal{H}_1 and \mathcal{H}_2 . As in the case of pure states, if ρ is not separable then it is entangled.

Consider a mixed state ρ on \mathcal{H}_t given by

$$\rho = \rho_{kl}^{ij} (|\psi_i\rangle \langle \psi_j|) \otimes (|\phi_k\rangle \langle \phi_l|) \quad (1.3)$$

where $|\psi_i\rangle$ and $|\phi_k\rangle$ are orthonormal bases for \mathcal{H}_1 and \mathcal{H}_2 and we have employed Einstein summation notation to sum over repeated indices. We define the partial

transpose state ρ^T by

$$\rho^T = \rho_{kl}^{ij} (|\psi_i\rangle \langle \psi_j|) \otimes (|\phi_l\rangle \langle \phi_k|) \quad (1.4)$$

The Peres-Horodecki criterion tells us that if the state ρ is separable then ρ^T has no negative eigenvalues when considered as an operator on \mathcal{H}_t . For arbitrary \mathcal{H}_1 and \mathcal{H}_2 there may be entangled states ρ which do not have negative eigenvalues, but for \mathcal{H}_t of dimension 2×2 and 2×3 it can be shown that for every entangled mixed state ρ the partial transpose ρ^T has a negative eigenvalue. The Peres-Horodecki criterion can also be restated in terms of a quantity \mathcal{N} called the negativity, where \mathcal{N} is the sum of the absolute values of the negative eigenvalues of ρ^T . If the negativity of a state is non-zero, then the state is entangled.

1.2 Unruh-DeWitt Detectors

Consider a free quantum scalar field ϕ defined on Minkowski space whose states are unit vectors in the Hilbert space $\mathcal{H}_{\text{field}}$ and whose Hamiltonian is \hat{H}_{field} . In order to model[14] the interaction of the field with a local particle detector, consider a detector whose internal state space $\mathcal{H}_{\text{detector}}$ is of dimension 2 and which moves along a predetermined worldline $(\tau, \vec{x}(\tau))$ parameterized by the detector's proper time τ . In the absence of interactions with the field, let the internal Hamiltonian of the detector be given by

$$\hat{H}_{\text{detector}} = \frac{\Omega}{2} (|\uparrow\rangle \langle \uparrow| - |\downarrow\rangle \langle \downarrow|) \quad (1.5)$$

so that the energy eigenstates $|\uparrow\rangle, |\downarrow\rangle$ have eigenvalues $\pm\Omega/2$. The combined system of field and detector has a Hilbert space $\mathcal{H}_{\text{field}} \otimes \mathcal{H}_{\text{detector}}$. Let the overall Hamiltonian of the system \hat{H}_t be

$$\hat{H}_t = \hat{H}_{\text{field}} \otimes 1 + 1 \otimes \hat{H}_{\text{detector}} + \hat{H}_{\text{interaction}} = \hat{H}_0 + \hat{H}_{\text{interaction}} \quad (1.6)$$

where

$$\hat{H}_{\text{interaction}}(\tau) = \eta(\tau) \hat{\phi}(x(\tau)) (|\uparrow\rangle \langle\downarrow| + |\downarrow\rangle \langle\uparrow|) \quad (1.7)$$

and $\eta(\tau)$ is a window function describing the time profile of the strength of the coupling between the field and detector. For weak interactions, first order time dependent perturbation theory in the interaction picture yields the transition amplitude for a field-detector system starting in the ground state $|0\rangle |\downarrow\rangle$ at $\tau = -\infty$ winding up in an excited state of the detector $|\phi_1\rangle |\uparrow\rangle$ for some field-state $|\phi_1\rangle$ at $\tau = \infty$. The transition amplitude is

$$\mathcal{T}_{\phi_1} = \int_{-\infty}^{\infty} d\tau \langle\phi_1| e^{i\hat{H}_0(\tau)} \hat{H}_{\text{interaction}} e^{-i\hat{H}_0\tau} |0\rangle. \quad (1.8)$$

or

$$\mathcal{T}_{\vec{k}} = \int_{-\infty}^{\infty} d\tau e^{i(E_{\vec{k}} + \Omega)\tau} \eta(\tau) \langle\vec{k}| \hat{\phi}(\vec{x}(\tau)) |0\rangle. \quad (1.9)$$

where I have made use of the fact that the state $|\phi_1\rangle$ must be a single-particle state $|\vec{k}\rangle$ of the field if the matrix element is to be nonzero, Ω is the energy difference between ground and excited states in the detector, and $E_{\vec{k}} = \sqrt{m^2 + \vec{k}^2}$ is the energy of the

field in a state $|\vec{k}\rangle$ with a single particle of momentum \vec{k} in the field. Calculating,

$$\hat{\phi}(\vec{x}(\tau))|0\rangle = \int \frac{d^3\vec{p}}{(2\pi)^3} \frac{1}{\sqrt{2E_{\vec{p}}}} e^{-i\vec{p}\cdot\vec{x}(\tau)} |\vec{p}\rangle \quad (1.10)$$

so that

$$\mathcal{T}_{\vec{k}} = \int_{-\infty}^{\infty} d\tau \int \frac{d^3\vec{p}}{(2\pi)^3} \frac{1}{\sqrt{2E_{\vec{p}}}} e^{i(E_{\vec{k}}+\Omega)\tau} e^{-i\vec{p}\cdot\vec{x}(\tau)} \eta(\tau) \langle \vec{k} | \vec{p} \rangle. \quad (1.11)$$

Making use of the normalization $\langle \vec{k} | \vec{p} \rangle = (2\pi)^3 \delta^{(3)}(\vec{k} - \vec{p})$ yields

$$\mathcal{T}_{\vec{k}} = \int_{-\infty}^{\infty} d\tau \frac{\eta(\tau)}{\sqrt{2E_{\vec{k}}}} e^{i[(E_{\vec{k}}+\Omega)\tau - \vec{k}\cdot\vec{x}(\tau)]} \quad (1.12)$$

To find the total probability of transitioning to a state in which the detector is excited, integrate the probability density over all \vec{k} to get

$$\mathcal{F} = \int d^3\vec{k} |\mathcal{T}_{\vec{k}}|^2 \quad (1.13)$$

which can be re-written as

$$\mathcal{F} = \int_{-\infty}^{\infty} d\tau \int_{-\infty}^{\infty} d\tau' \eta(\tau) \eta(\tau') e^{-i\Omega(\tau-\tau')} \langle 0 | \hat{\phi}(x(\tau)) \hat{\phi}(x(\tau')) | 0 \rangle \quad (1.14)$$

The probability that the detector is excited is a function of the detector energy gap Ω , the worldline $\vec{x}(\tau)$, the window function $\eta(\tau)$, and the Wightman function $G_+(x, y) = \langle \phi(x) \phi(y) \rangle$ for the scalar field along its worldline. This expression for \mathcal{F} remains valid in spacetimes other than Minkowski space and for finite temperature by

replacing the Wightman function $G_+(x, y)$ of Minkowski space with the corresponding Wightman function for a field on a different spacetime or at non-zero temperature. Thus the behavior of Unruh-DeWitt detectors is connected to the global properties of spacetime which are encoded into the Wightman function, so that it is possible to probe the properties of spacetime via Unruh-DeWitt detectors.

1.3 Entanglement Harvesting

”Entanglement harvesting” is named for the possibility of harvesting[15] the resource of quantum entanglement from the field ϕ . If there are two Unruh-DeWitt detectors coupled to ϕ instead of only one, it is possible for the detectors to become entangled with one another via harvesting entanglement present in the vacuum state of ϕ . The possibility of entanglement harvesting from a scalar quantum field was first proposed by Reznik[16]. Reznik noted an interesting result— two Unruh-DeWitt detectors can become entangled with one another after interacting with ϕ even if the detectors are spacelike separated from one another at all points on their worldlines at which the detector is active, i.e. all points τ on the worldline for which the window function $\eta(\tau)$ is non-zero. Reznik also demonstrates that this is not just a result of the acceleration of the detectors by giving an example of stationary detectors which are spacelike separated and which become entangled with one another by interacting with ϕ .

Reznik’s results have been generalized to Minkowski space with finite temperature and de Sitter space[17][18]. The subset of the parameter space of the detectors for which entanglement develops between the detectors is seen to depend on both the tem-

perature and topology of the spacetime, demonstrating the ability of entanglement harvesting to reveal properties of spacetime. However, it has also been shown[19][20] that in the case of de Sitter space, a massless scalar field cannot induce entanglement between detectors which are separated by distances on the scale of the Hubble horizon. Other studies have shown the necessity of an energy gap in the detector for entanglement harvesting[21], analyzed the impact of using a harmonic oscillator as a detector rather than two-state system[22], the extension of entanglement harvesting from scalar fields to vector fields[23], and an interesting counterexample to the shell theorem of Newtonian gravity in which entanglement harvesting can be used to detect the presence of a hollow spherical shell surrounding a region of spacetime[24]. Direct violations of Bell’s inequality have also been exhibited as a result of entanglement harvesting[25]. Finally, there have been analyses of models in which the scalar field ϕ has been discretized[26][27][28].

In the next chapter of this thesis, I will extend the theory of entanglement harvesting to examine via numerical integration regions of the parameter space for Unruh-DeWitt detectors travelling with constant acceleration which were not included in previous results obtained via analytic approximation. An example of an analytical calculation of entanglement harvesting will be presented in Chapter 2 as a part of the discussion of entanglement harvesting in Minkowski space.

1.4 Gauss-Kronrod Quadrature

My results on entanglement harvesting require numerically integrating integrands which cannot be integrated analytically. Thus, it is necessary to explain the numerical integration algorithm used to obtain the results.

For the entanglement harvest calculation in Chapter 2, there are both one and two dimensional integrals which must be evaluated numerically. I convert the two dimensional integral into two nested one dimensional integrals using Fubini's theorem. To calculate the one dimensional integrals, I use the Gauss-Kronrod method as implemented in Wolfram Mathematica.

Gaussian Quadrature

The Gauss-Kronrod method is built upon the simpler method of Gaussian quadrature. Given a function $f(x)$, it is desirable for computational purposes to estimate the integral

$$I = \int_{-1}^1 dx f(x) \tag{1.15}$$

using only the values of $f(x)$ at a finite number N of points in $[-1, 1]$. Integrals on more general intervals $[a, b]$ can be evaluated by shifting and scaling the function to map $[a, b]$ to $[-1, 1]$. The integral is approximated as

$$I \approx I_{G,N} = \sum_{i=1}^N w_i f(x_i) \tag{1.16}$$

i	w_i	x_i
1	0.56889	0.00000
2	0.47863	-0.53847
3	0.47863	0.53847
4	0.23693	-0.90618
5	0.23693	0.90618

Table 1.1: Evaluation points and weighting coefficients for Gaussian quadrature with 5 points on $[-1,1]$.

for some weighting coefficients w_1, \dots, w_N and points x_1, \dots, x_N to be determined. The method of Gaussian quadrature for a given N arises from choosing w_i and x_i so as to ensure the approximation is exact for polynomials of degree $0 \leq k \leq 2N - 1$,

$$\int_{-1}^1 dx x^k = \sum_{i=1}^N w_i x_i^k \quad (1.17)$$

The points x_i can be shown[29] to be located at the roots of the N th Legendre polynomial $P_N(x)$, while the weights can be shown to satisfy

$$w_i = \frac{2}{(1 - x_i^2)[P'_N(x_i)]^2} \quad (1.18)$$

For the numerical integrations in this thesis, the Gaussian quadrature subroutine of the Gauss-Kronrod method uses $N = 5$, corresponding to the points shown in Table 1.1.

Although Gaussian quadrature has theoretical error bound proportional to $f^{(2N)}(\xi)$ for some ξ in $[-1, 1]$, this estimate is not always useful in practice. For many functions $f(x)$ it is not possible to accurately evaluate $f^{(2N)}$ for large N in order to obtain the error bound, and there are many situations in which the theoretical error bound

greatly overestimates the amount of error. The need for a better error estimate motivates the extension of Gaussian quadrature to the Gauss-Kronrod method.

Gauss-Kronrod Quadrature

The Gauss-Kronrod quadrature algorithm[30] provides an error estimate for Gaussian quadrature $I_{G,N}$ of $f(x)$ by comparing it to $I_{GK,2N+1}$, the result of numerical integration which uses additional points in $[-1,1]$. The error estimate for $I_{G,N}$ is then given by $(200|I_{G,N} - I_{GK,2N+1}|)^{1.5}$.

In particular, the Gauss-Kronrod algorithm builds on the N -point Gaussian quadrature by introducing $N + 1$ extra points x_{N+1}, \dots, x_{2N+1} at which the function f will be evaluated. The points y_i are chosen to be the roots of the Stieltjes polynomial $E_{N+1}(x)$, while the weights are chosen so that $I = I_{GK,2N+1}$ when $f(x)$ is polynomial of degree at most $3N + 1$. The original points x_1, \dots, x_N are re-used so as to require calculating only $N + 1$ new function values $f(x_i)$ for $i = N + 1, \dots, 2N + 1$. For the case of $N = 5$, the points and weights are shown in Table 1.2. The error estimate provided by Gauss-Kronrod method allows for its use by adaptive integration algorithms. Mathematica[31] has two adaptive integration algorithms which it can use with the Gauss-Kronrod algorithm corresponding to the LocalAdaptive and GlobalAdaptive of the NIntegrate command. Both strategies divide up the domain of integration into intervals recursively, using Gauss-Kronrod quadrature to calculate the integral and an error estimate and sub-dividing intervals for which the error estimate is too large. The GlobalAdaptive strategy stops when the relative error estimate for the

i	w_i	x_i
1	0.04258	-0.98408
2	0.11523	-0.90618
3	0.18680	-0.75417
4	0.24104	-0.53847
5	0.27285	-0.27963
6	0.28299	0.00000
7	0.27285	0.27963
8	0.24104	0.53847
9	0.18680	0.75417
10	0.11523	0.90618
11	0.04258	0.98408

Table 1.2: Evaluation points and weighting coefficients for Gauss-Kronrod quadrature with 11 points on $[-1,1]$.

integral as a whole is sufficiently small (as determined by Mathematica's precision settings), while the "LocalAdaptive" strategy subdivides intervals until the relative error estimate for the integral on each interval is sufficiently small.

The infinite domain of integration is handled by the observation that the integrands I will integrate decay exponentially with $|x|$ as $x \rightarrow \pm\infty$, so an integral over \mathbb{R} can be approximated to arbitrary accuracy by integrating over $[-L, L]$ for large values of L .

Chapter 2

Numerical Evaluation of Acceleration-Assisted Entanglement Harvesting

2.1 Introduction to the Problem

Over the last few years, there has been investigation into entanglement harvesting [32] [19] [18] [17] [33] [16]: a phenomenon, most easily realized in models containing a scalar field coupled to multiple (usually two) separated Unruh-DeWitt detectors, in which, for certain choices of the detectors' worldlines, they can become quantum entangled. In a sense, the entangled nature of the vacuum state of a scalar field can be transferred to detectors with appropriate interactions and executing suitable motions.

Entanglement harvesting is a beautiful illustration of how the infectious nature of

entanglement allows interactions to readily spread this iconic quantum characteristic. Moreover, entanglement harvesting provides a simple laboratory to study how the degree to which two objects – in this case, two Unruh-DeWitt detectors – become entangled depends on detailed physical features including the accelerations of the detectors, the mass gap of each detector, and the distance between them.

In Salton, et al. [32], the authors used the by now standard measure of entanglement, negativity, to quantify the entanglement between two accelerating Unruh-DeWitt detectors. Using repeated stationary phase approximations, the authors found the region in the space of coefficients (c_1, c_2) for which the Unruh-DeWitt detectors would become entangled, where $c_1 = \kappa L$, and $c_2 = \kappa \Omega \sigma^2$, where κ describes the relative acceleration, L the separation and Ω the energy splitting in a pair of two state Unruh detectors. Of particular note, in the stationary phase approximation invoked, the parameter $c_3 = \sigma \Omega$, with σ denoting the half width of a Gaussian window function specifying the field-detector interaction, only enters as an overall factor in the negativity and hence plays no role in determining its sign (and thus whether entanglement has been transferred to the detectors). I go beyond the stationary phase approximation using numerical integration to compute the non-trivial c_3 dependence of the negativity.

2.2 Basic Set-Up of Detectors

The simplest setting to study entanglement harvesting is that of two accelerating Unruh-DeWitt detectors labeled A and B . As discussed in Chapter 1, each is de-

scribed by a two-state Hamiltonian H_{det_i} of the form

$$\hat{H}_{\text{det}_i} = \frac{\Omega}{2} (|\uparrow\rangle\langle\uparrow| - |\downarrow\rangle\langle\downarrow|) \quad (2.1)$$

acting on the detector Hilbert spaces $\mathcal{H}_{\text{det}_i}$ and each detector is coupled to the same scalar field ϕ through an interaction Hamiltonian

$$\hat{H}_{\text{int}_i} = \eta(\tau)\hat{\phi}(x_i(\tau)) (|\uparrow\rangle\langle\downarrow| + |\downarrow\rangle\langle\uparrow|) \quad (2.2)$$

where $x_i(\tau)$ parameterizes the worldline of detector i ($i = A, B$) in terms of the detector's proper time τ . We envision that the Unruh-DeWitt detectors are travelling along worldlines with constant acceleration either parallel or anti-parallel to one another. In such a model, the overall Hilbert space is $\mathcal{H}_\phi \otimes \mathcal{H}_{\text{det}_A} \otimes \mathcal{H}_{\text{det}_B}$ and the Hamiltonian is given by

$$\hat{H} = \hat{H}_\phi + \hat{H}_{\text{det}_A} + \hat{H}_{\text{det}_B} + \hat{H}_{\text{int}_A} + \hat{H}_{\text{int}_B} \quad (2.3)$$

where \hat{H}_{det_i} and \hat{H}_{int_i} represent the internal Hamiltonians of the detectors and interaction Hamiltonians respectively, and we have suppressed trivial tensor products (e.g. $\hat{H}_\phi \otimes 1 \otimes 1 = \hat{H}_\phi$) for simplicity. Switching to the interaction picture, we find that the interaction Hamiltonian is again the sum of the Hamiltonians for each individual detector. We calculate the final state of the system at $\tau = \infty$ after starting in the

state $|0\rangle |\downarrow_A\rangle |\downarrow_B\rangle$ at $\tau = -\infty$. Define the operators $\hat{\Phi}_i^\pm$ for $i = A, B$ by

$$\hat{\Phi}_i^\pm = \int_{-\infty}^{\infty} d\tau' \eta(\tau') e^{\pm i\Omega\tau'} \hat{\phi}(x_i(\tau')) \quad (2.4)$$

Now define an operator \hat{S} by

$$\hat{S} = -i \sum_{i=A,B} \sum_{j=+,-} \hat{\Phi}_i^j \sigma_i^j \quad (2.5)$$

where $\sigma_i^+ = |\uparrow_i\rangle \langle \downarrow_i|$ and $\sigma_i^- = |\downarrow_i\rangle \langle \uparrow_i|$. Note that

$$\begin{aligned} \hat{S}^2 = & - (\hat{\Phi}_A^- \hat{\Phi}_A^+ + \hat{\Phi}_B^- \hat{\Phi}_B^+ + \hat{\Phi}_B^+ \hat{\Phi}_A^+ |\uparrow_A\rangle |\uparrow_B\rangle \langle \downarrow_A| \langle \downarrow_B| \\ & + \hat{\Phi}_A^+ \hat{\Phi}_B^+ |\uparrow_A\rangle |\uparrow_B\rangle \langle \downarrow_A| \langle \downarrow_B|) + (\text{irrelevant terms}) \end{aligned} \quad (2.6)$$

where "irrelevant terms" refers to terms which vanish when considering the action of S^2 on the ground state of the system.

The time evolution operator in the interaction picture is then given by $\mathcal{T} [e^{\hat{S}}]$ where \mathcal{T} is the time-ordering symbol, so that to second order in perturbation theory the state $|\psi\rangle$ at $\tau = \infty$ is given by

$$\begin{aligned} |\psi\rangle = & \left(1 + \hat{S} + \frac{1}{2} \mathcal{T} [\hat{S}\hat{S}] \right) |0\rangle |\downarrow_A\rangle |\downarrow_B\rangle \\ |\psi\rangle = & (1 + d_1) |0\rangle |\downarrow_A\rangle |\downarrow_B\rangle - i \left(\hat{\Phi}_A^+ |0\rangle |\uparrow_A\rangle |\downarrow_B\rangle + \hat{\Phi}_B^+ |0\rangle |\downarrow_A\rangle |\uparrow_B\rangle \right) \\ & - \frac{1}{2} \mathcal{T} \left[\hat{\Phi}_A^+ \hat{\Phi}_B^+ + \hat{\Phi}_B^+ \hat{\Phi}_A^+ \right] |0\rangle |\uparrow_A\rangle |\uparrow_B\rangle \end{aligned} \quad (2.7)$$

where we have defined $d_1 = -\frac{1}{2} \langle 0 | \mathcal{T} \left[\hat{\Phi}_A^- \hat{\Phi}_A^+ + \hat{\Phi}_B^- \hat{\Phi}_B^+ \right] |0\rangle$.

We find the density matrix corresponding to this pure state to second order in perturbation theory. Keeping only terms with at most two $\hat{\Phi}_j^k$ factors in them and which are nonvanishing after taking partial trace over \mathcal{H}_ϕ , we obtain

$$\begin{aligned}
\rho = |\psi\rangle\langle\psi| = & (1 + d_1 + d_1^*) |0\rangle|\downarrow_A\rangle|\downarrow_B\rangle\langle 0|\langle\downarrow_A|\langle\downarrow_B| \\
& - \hat{\Phi}_A^+ \hat{\Phi}_B^+ |0\rangle|\uparrow_A\rangle|\uparrow_B\rangle\langle 0|\langle\downarrow_A|\langle\downarrow_B| \\
& - |0\rangle|\downarrow_A\rangle|\downarrow_B\rangle \left(\langle 0|\hat{\Phi}_B^- \hat{\Phi}_A^- \right) \langle\uparrow_A|\langle\uparrow_B| \\
& - \hat{\Phi}_A^+ |0\rangle|\uparrow_A\rangle|\downarrow_B\rangle \left(\langle 0|\hat{\Phi}_A^- \right) \langle\uparrow_A|\langle\downarrow_B| \\
& - \hat{\Phi}_B^+ |0\rangle|\downarrow_A\rangle|\uparrow_B\rangle \left(\langle 0|\hat{\Phi}_B^- \right) \langle\downarrow_A|\langle\uparrow_B| \\
& - \hat{\Phi}_A^+ |0\rangle|\uparrow_A\rangle|\downarrow_B\rangle \left(\langle 0|\hat{\Phi}_B^- \right) \langle\downarrow_A|\langle\uparrow_B| \\
& - \hat{\Phi}_B^+ |0\rangle|\downarrow_A\rangle|\uparrow_B\rangle \left(\langle 0|\hat{\Phi}_A^- \right) \langle\uparrow_A|\langle\downarrow_B|
\end{aligned} \tag{2.8}$$

which, after partial tracing, becomes

$$\begin{aligned}
\rho_{\text{tr}} = |\psi\rangle\langle\psi| = & (1 + d_1 + d_1^*) |\downarrow_A\rangle|\downarrow_B\rangle\langle\downarrow_A|\langle\downarrow_B| \\
& - \left\langle 0|\hat{\Phi}_A^+ \hat{\Phi}_B^+ |0\rangle \right\rangle |\uparrow_A\rangle|\uparrow_B\rangle\langle\downarrow_A|\langle\downarrow_B| \\
& - \left\langle 0|\hat{\Phi}_A^+ \hat{\Phi}_B^+ |0\rangle \right\rangle^* |\downarrow_A\rangle|\downarrow_B\rangle\langle\uparrow_A|\langle\uparrow_B| \\
& - \left\langle 0|\hat{\Phi}_A^- \hat{\Phi}_A^+ |0\rangle \right\rangle |\uparrow_A\rangle|\downarrow_B\rangle\langle\uparrow_A|\langle\downarrow_B| \\
& - \left\langle 0|\hat{\Phi}_B^- \hat{\Phi}_B^+ |0\rangle \right\rangle |\downarrow_A\rangle|\uparrow_B\rangle\langle\downarrow_A|\langle\uparrow_B| \\
& - \left\langle 0|\hat{\Phi}_B^- \hat{\Phi}_A^+ |0\rangle \right\rangle |\uparrow_A\rangle|\downarrow_B\rangle\langle\downarrow_A|\langle\uparrow_B| \\
& - \left\langle 0|\hat{\Phi}_B^+ \hat{\Phi}_A^- |0\rangle \right\rangle |\downarrow_A\rangle|\uparrow_B\rangle\langle\uparrow_A|\langle\downarrow_B|
\end{aligned} \tag{2.9}$$

Writing this in matrix form, we find

$$\rho_{\text{tr}} = \begin{pmatrix} 1 - \langle 0 | \hat{\Phi}_A^- \hat{\Phi}_A^+ + \hat{\Phi}_B^- \hat{\Phi}_B^+ | 0 \rangle & - \langle 0 | \hat{\Phi}_A^+ \hat{\Phi}_B^+ | 0 \rangle & 0 & 0 \\ - \langle 0 | \hat{\Phi}_A^+ \hat{\Phi}_B^+ | 0 \rangle & 0 & 0 & 0 \\ 0 & 0 & \langle 0 | \hat{\Phi}_A^- \hat{\Phi}_A^+ | 0 \rangle & \langle 0 | \hat{\Phi}_B^- \hat{\Phi}_B^+ | 0 \rangle \\ 0 & 0 & \langle 0 | \hat{\Phi}_A^- \hat{\Phi}_B^+ | 0 \rangle & \langle 0 | \hat{\Phi}_B^- \hat{\Phi}_B^+ | 0 \rangle \end{pmatrix} \quad (2.10)$$

We define

$$E_A = \langle 0 | \hat{\Phi}_A^- \hat{\Phi}_A^+ | 0 \rangle = \int_{-\infty}^{\infty} d\tau' \int_{-\infty}^{\infty} d\tau'' \eta(\tau') \eta(\tau'') e^{i\Omega(\tau' - \tau'')} G_+(x_A(\tau'), x_A(\tau'')) \quad (2.11)$$

$$E_B = \langle 0 | \hat{\Phi}_B^- \hat{\Phi}_B^+ | 0 \rangle = \int_{-\infty}^{\infty} d\tau' \int_{-\infty}^{\infty} d\tau'' \eta(\tau') \eta(\tau'') e^{i\Omega(\tau' - \tau'')} G_+(x_B(\tau'), x_B(\tau'')) \quad (2.12)$$

$$X = \langle 0 | \hat{\Phi}_A^+ \hat{\Phi}_B^+ | 0 \rangle = \int_{-\infty}^{\infty} d\tau' \int_{-\infty}^{\tau'} d\tau'' \eta(\tau') \eta(\tau'') e^{i\Omega(\tau' + \tau'')} G_+(x_A(\tau'), x_B(\tau'')) \quad (2.13)$$

where G_+ is the Wightman function for ϕ and we have made use of the symmetry under exchanging $\tau' \leftrightarrow \tau''$ to rewrite the E_i integrals as being over the entire $\tau' - \tau''$ plane.

Parallel Worldlines

Salton et al. investigate a situation in which two detectors with constant separation move with constant acceleration. A massless field ϕ is coupled to two detectors with worldlines denoted by $x_A(\tau)$ and $x_B(\tau)$. The detector worldlines are of the form

$$x_A(\tau) = (t = \frac{1}{\kappa} \sinh \kappa \tau, x = \frac{1}{\kappa} (\cosh \kappa \tau - 1), y = 0, z = 0) \quad (2.14)$$

$$x_B(\tau) = \left(t = \frac{1}{\kappa} \sinh \kappa \tau, x = \frac{1}{\kappa} (\cosh \kappa \tau - 1) + L, y = 0, z = 0 \right) \quad (2.15)$$

and the Wightman function for a massless field ϕ is given by

$$G_+(x, y) = -\frac{1}{(2\pi)^2} \frac{1}{(x - y)^2} \quad (2.16)$$

where we have the pole prescription $(x - y)^2 = (x_0 - y_0 - i\epsilon)^2 - (\vec{x} - \vec{y})^2$ for the Wightman function. These choices lead to the integrals (in this case, $E_A = E_B = E$)

$$E = -\frac{\kappa^2}{4\pi^2} \int_{-\infty}^{\infty} d\tau' \int_{-\infty}^{\infty} d\tau'' \exp \left[-\frac{(\tau'^2 + \tau''^2)}{2\sigma^2} - i\Omega(\tau' - \tau'') \right] \times \frac{1}{(\sinh \kappa \tau' - \sinh \kappa \tau'')^2 - (\cosh \kappa \tau' - \cosh \kappa \tau'')^2} \quad (2.17)$$

$$X = -\frac{\kappa^2}{4\pi^2} \int_{-\infty}^{\infty} d\tau' \int_{-\infty}^{\tau'} d\tau'' \exp \left(-\frac{\tau'^2 + \tau''^2}{2\sigma^2} + i\Omega(\tau' + \tau'') \right) \times \frac{1}{(\sinh \kappa \tau' - \sinh \kappa \tau'')^2 - (\cosh \kappa \tau' - \cosh \kappa \tau'' - L\kappa)^2} \quad (2.18)$$

Defining $x = \tau' + \tau''$ and $y = \tau' - \tau''$, after some algebraic manipulation (and reinserting the ϵ defining the pole prescription for clarity) the integrals can be rewritten as

$$E = -\frac{\kappa^2 \eta_0^2}{32\pi^2} e^{-\sigma^2 \Omega^2} \int_{-\infty}^{\infty} dx \int_{-\infty}^{\infty} dy \exp \left[-\frac{1}{4\sigma^2} (x^2 + (y + 2i\Omega\sigma^2)^2) \right] \text{csch}^2 \left(\frac{\kappa y}{2} \right) \quad (2.19)$$

$$X = \frac{\kappa^2 \eta_0^2}{32\pi^2} e^{-\sigma^2 \Omega^2} \int_{-\infty}^{\infty} dx \int_0^{\infty} dy \exp \left(-\frac{(x - 2i\Omega\sigma^2)^2 + y^2}{4\sigma^2} \right) \times \left[\frac{L\kappa}{2} + i\epsilon - e^{-\kappa x/2} \sinh \left(\frac{\kappa y}{2} \right) \right]^{-1} \left[\frac{L\kappa}{2} - i\epsilon + e^{\kappa x/2} \sinh \left(\frac{\kappa y}{2} \right) \right]^{-1} \quad (2.20)$$

Introducing the dimensionless parameters $c_1 = \kappa L$, $c_2 = \kappa \Omega \sigma^2$, and $c_3 = \sigma \Omega$ and substituting $\tilde{x} = x/L$ and $\tilde{y} = y/L$, we obtain

$$E = -\eta_0^2 \frac{c_1^2}{32\pi^2} e^{-c_3^2} \int_{-\infty}^{\infty} d\tilde{x} \int_{-\infty}^{\infty} d\tilde{y} \exp \left[- \left(\frac{c_1 c_3}{2c_2} \right)^2 (\tilde{x}^2 + (\tilde{y} + 2ic_2/c_1)^2) \right] \operatorname{csch}^2 \left(\frac{c_1 \tilde{y}}{2} \right) \quad (2.21)$$

$$X = \eta_0^2 \frac{c_1^2}{32\pi^2} e^{-c_3^2} \int_{-\infty}^{\infty} d\tilde{x} \int_0^{\infty} d\tilde{y} \exp \left(- \left(\frac{c_1 c_3}{2c_2} \right)^2 ((\tilde{x} - 2ic_2/c_1)^2 + \tilde{y}^2) \right) \\ \times \left[\frac{c_1}{2} + i\epsilon - e^{-c_1 \tilde{x}/2} \sinh \left(\frac{c_1 \tilde{y}}{2} \right) \right]^{-1} \left[\frac{c_1}{2} - i\epsilon + e^{c_1 x/2} \sinh \left(\frac{c_1 y}{2} \right) \right]^{-1} \quad (2.22)$$

These integrals can be made easier to evaluate by shifting the contour of integration in the complex plane. In the case of E , let the contour shift from integrating \tilde{y} along the real axis to integrating along the line $y = y' - 2ic_2/c_1$ where y' ranges from $-\infty$ to ∞ . In the case of X , shift from integrating x along the real axis to integrating along the line $\tilde{x} = x' + 2ic_2/c_1$ where y' ranges from $-\infty$ to ∞ . Note that this justifies neglecting the $i\epsilon$ in the denominators, since the integrals are no longer crossing poles.

The resulting integrals are

$$E = -\eta_0^2 \frac{c_1^2}{32\pi^2} e^{-c_3^2} \int_{-\infty}^{\infty} d\tilde{x} \int_{-\infty}^{\infty} d\tilde{y} \exp \left[- \left(\frac{c_1 c_3}{2c_2} \right)^2 (\tilde{x}^2 + \tilde{y}^2) \right] \operatorname{csch}^2 \left(\frac{c_1 \tilde{y}}{2} - ic_2 \right) \quad (2.23)$$

$$X = \eta_0^2 \frac{c_1^2}{32\pi^2} e^{-c_3^2} \int_{-\infty}^{\infty} d\tilde{x} \int_0^{\infty} d\tilde{y} \exp \left(- \left(\frac{c_1 c_3}{2c_2} \right)^2 (\tilde{x}^2 + \tilde{y}^2) \right) \\ \times \left[\frac{c_1}{2} + i\epsilon - e^{-c_1 \tilde{x}/2} e^{-ic_2} \sinh \left(\frac{c_1 \tilde{y}}{2} \right) \right]^{-1} \left[\frac{c_1}{2} - i\epsilon + e^{c_1 x/2} e^{ic_2} \sinh \left(\frac{c_1 y}{2} \right) \right]^{-1} \quad (2.24)$$

The expression for E can be further simplified by noting that the integral over \tilde{x} is purely Gaussian. Carrying out the \tilde{x} -integral yields

$$E = -\eta_0^2 \frac{c_1}{16\pi^{3/2}} \frac{c_2}{c_3} e^{-c_3^2} \int_{-\infty}^{\infty} d\tilde{y} \exp \left[-\left(\frac{c_1 c_3}{2c_2} \right)^2 \tilde{y}^2 \right] \operatorname{csch}^2 \left(\frac{c_1 \tilde{y}}{2} - i c_2 \right) \quad (2.25)$$

The paper by Salton et al. uses the stationary phase approximation on both of these integrals. Given our shift of variables, this is equivalent to replacing the factor $f(x, y)$ multiplying the Gaussian in each by $f(0, 0)$. This gives

$$E_{\text{sp}} = \eta_0^2 \frac{e^{-c_3^2}}{8\pi} \left(\frac{c_2}{c_3} \right)^2 \operatorname{csc}^2 c_2 \quad (2.26)$$

$$X_{\text{sp}} = \eta_0^2 \frac{e^{-c_3^2}}{2\pi} \left(\frac{c_2}{c_3 c_1} \right)^2 \quad (2.27)$$

for the integrals. Whether the detectors are entangled is determined by calculating whether the negativity \mathcal{N} of the system described by ρ_{tr} is non-zero. The negativity, discussed as means for measuring entanglement in Chapter 1, is given in this situation by

$$\mathcal{N} = \max\{|X| - E, 0\} = \eta_0^2 \frac{e^{-c_3^2}}{8\pi} \left(\frac{c_2}{c_3} \right)^2 \left[\frac{4}{c_1^2} - \operatorname{csc}^2 c_2 \right] \quad (2.28)$$

In this approximation c_3 only enters in an overall factor and so has no impact on the sign of \mathcal{N} .

For large values of c_3 , the Gaussian factor in the integrands for both E and X suppresses the integrand everywhere except for the point ($\tilde{x} = 0, \tilde{y} = 0$). This suggests that for large c_3 , we should obtain the same result as we would obtain

using the stationary phase approximation. Physically, for fixed c_1, c_2 we find that c_3 parameterizes the width of the window function Gaussian and so the amount of time the detectors have to interact with each other. This leads to the expectation that for small c_3 there will not be enough time for entanglement to be established, while for large c_3 the presence of entanglement is dependent on the parameters governing the choice of detector worldlines.

2.3 Numerical Evaluation

I numerically evaluated the integrals for E and X for the range of parameter space $c_1 \in [0, 6]$, $c_2 \in [0, 3]$, $c_3 \in [0, 5]$, using Wolfram Mathematica. For E , the single integral can be evaluated straightforwardly using a Gauss-Kronrod method with $N = 5$ points. For X , using the default “GlobalAdaptive” strategy and evaluating the integral as two nested single variable integrals each using the Gauss-Kronrod method, Mathematica warns about possible inaccuracy when evaluating the integral for some parameters within the chosen parameter space. Although Mathematica reports a guess for the error on these numerical integrals, there is no guarantee that the guess will not greatly underestimate the true amount of error.

I provide my own estimate of the amount of error by doing the integrations using Mathematica’s “LocalAdaptive” strategy rather than its default “GlobalAdaptive” strategy. As discussed in Chapter 1, both strategies in this case compute numerical integrals by recursively dividing up the integration region into subregions and using a Gauss-Kronrod method to estimate the integral value and error. However, the

“LocalAdaptive” strategy makes its choice of which subregion to further divide via a local estimate of the integration error in that region, while “GlobalAdaptive” chooses which subregions to refine based on the magnitude of error compared to the overall value of the integral. This makes the LocalAdaptive more sensitive to oscillatory behavior in the integrands at the cost of increasing the number of subdivisions of the domain used in the computation.

I calculated the values of E and X on the 3D grid in parameter space on which the parameters take on the values $c_1 = \{0.025, 0.050, 0.075, \dots, 5.975, 6.000\}$, $c_2 = \{0.025, 0.050, 0.075, \dots, 3.000\}$, $c_3 = \{0.125, 0.250, \dots, 4.875, 5.000\}$ using the “LocalAdaptive” integration strategy. We also calculated X using the “GlobalAdaptive” strategy on the same grid to compare with the “LocalAdaptive” results.

We then used the values of E and X to calculate $\mathcal{N}_0 = |X| - E$, which equals the negativity \mathcal{N} when $\mathcal{N}_0 < 0$. The sign of \mathcal{N}_0 determine which regions of parameter space support entanglement. The regions are shown in Figure 2.1 through Figure 2.5.

I calculated the difference between the “LocalAdaptive” and “GlobalAdaptive” results for both the values of E and X as well as the final negativity result \mathcal{N}_0 . We found that the values for X matched to within 0.08% and for \mathcal{N}_0 to within 9%.

Collectively, these calculations paint a picture of the dependence of the entanglement region on c_3 . In the limit as c_3 approaches 0, the entanglement region vanishes, while for $c_3 \geq 4.5$ the entanglement region looks similar to that computed by Salton et al. This is consistent with the expectation that the stationary phase approximation integrals for E and X should be accurate for large c_3 .

2.4 Discussion

A natural next step in this line of research is to extend the analysis to more general trajectories, including the antiparallel case, and, of significant interest to a complete analysis, to consider the effect of different window functions. The latter could establish that the Gaussian tails of the window functions currently in use play no essential role in the entanglement results, as suggested by Reznik[33]. It would also be useful to examine other choices of Wightman function $G_+(x, y)$ corresponding to spacetimes of different topology or at finite temperature. I intend to return to these undertakings in future work.

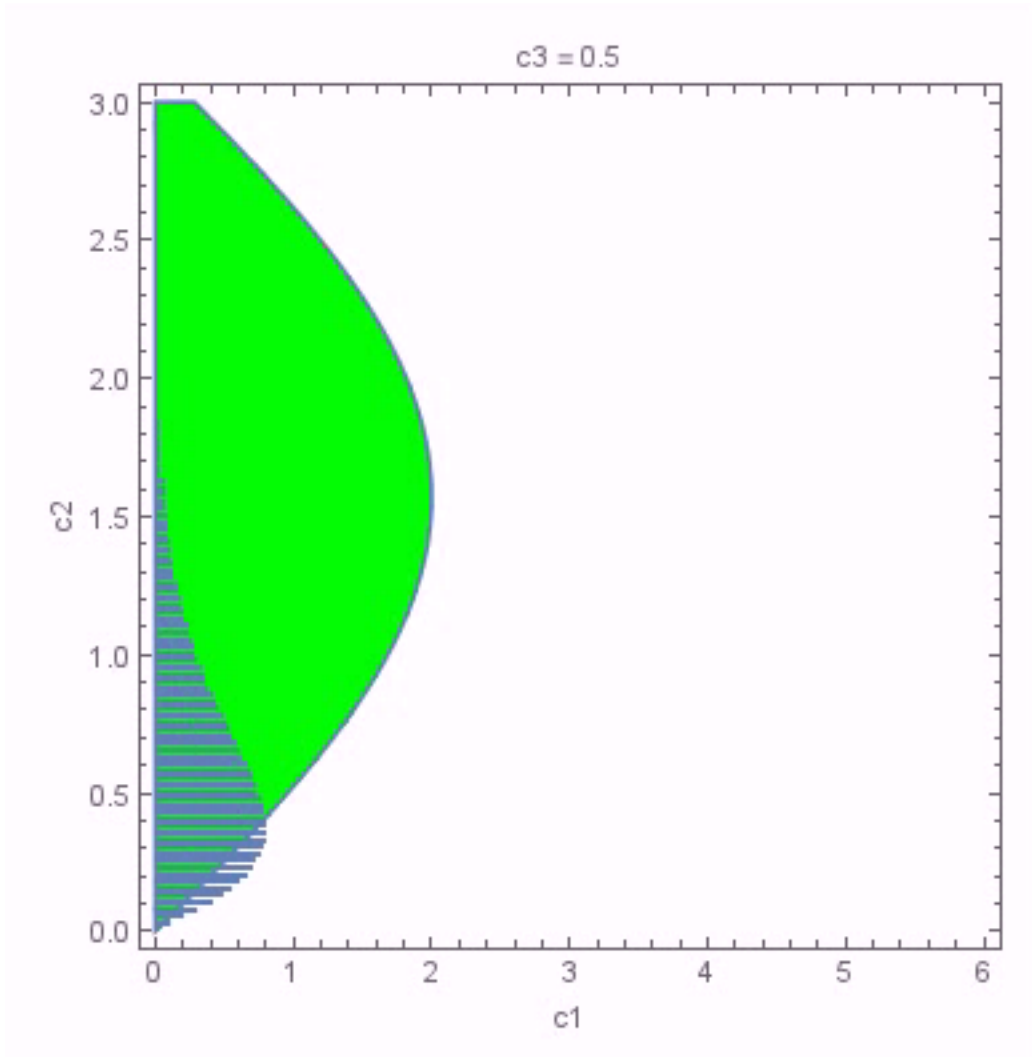


Figure 2.1: Region of parameter space which support entanglement harvesting which supports entanglement harvesting for $c_3 = 0.5$. The green region is calculated with the stationary phase approximation, while the region defined by blue dots is calculated numerically.

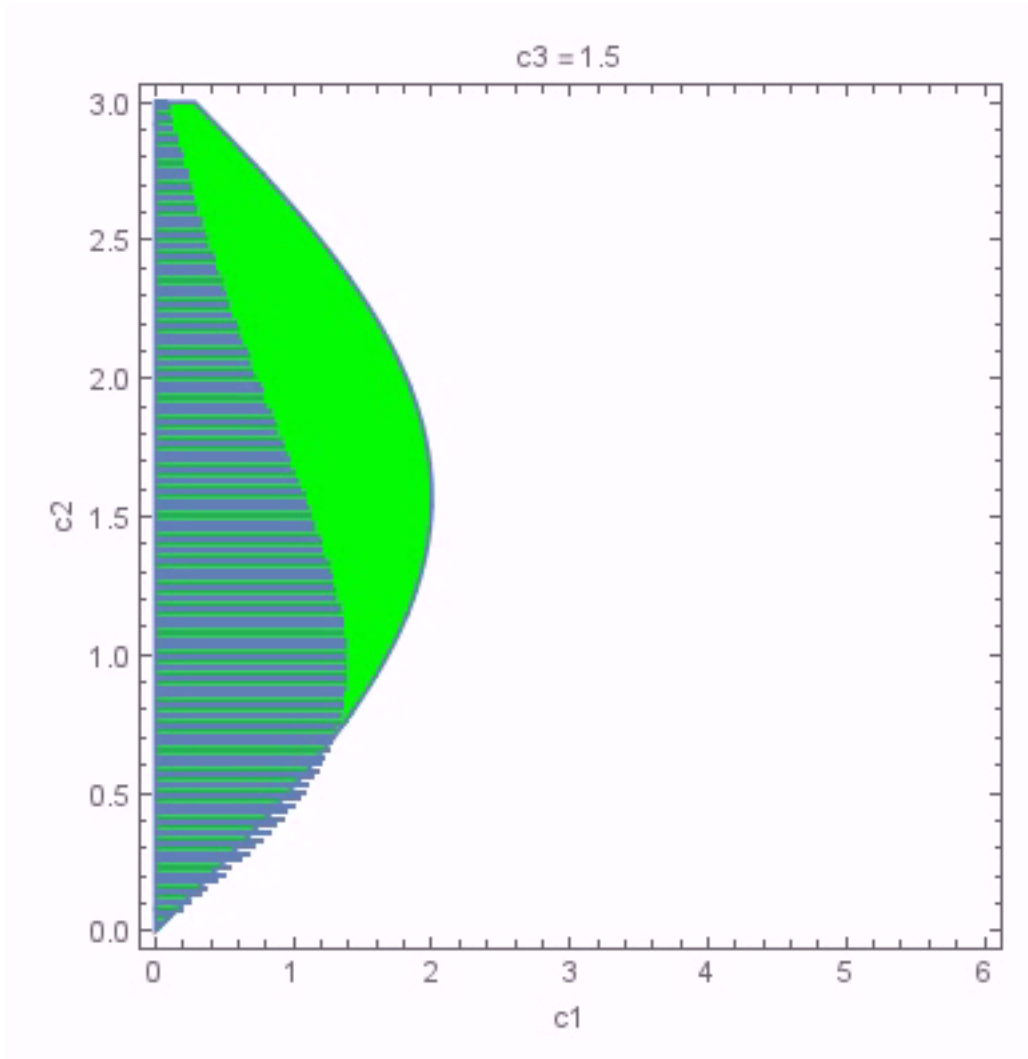


Figure 2.2: Region of parameter space which support entanglement harvesting which supports entanglement harvesting for $c_3 = 1.5$. The green region is calculated with the stationary phase approximation, while the region defined by blue dots is calculated numerically.

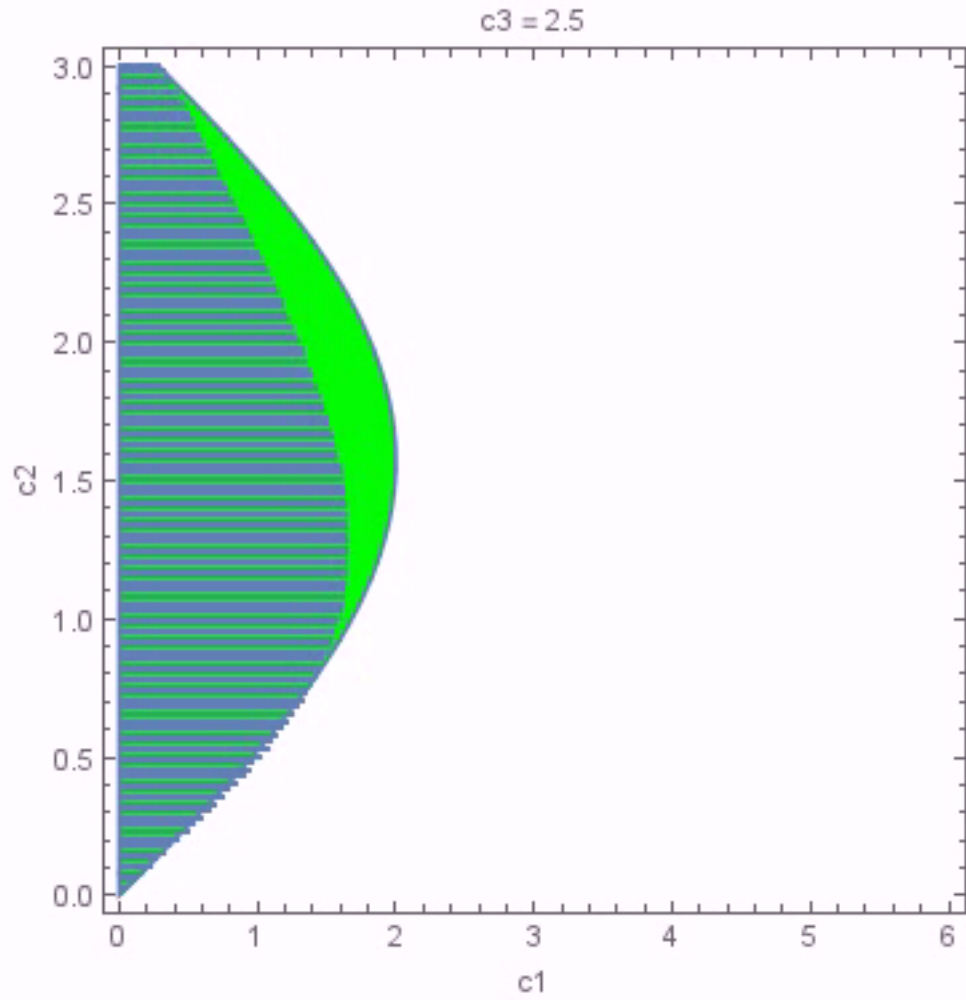


Figure 2.3: Region of parameter space which support entanglement harvesting which supports entanglement harvesting for $c_3 = 2.5$. The green region is calculated with the stationary phase approximation, while the region defined by blue dots is calculated numerically.

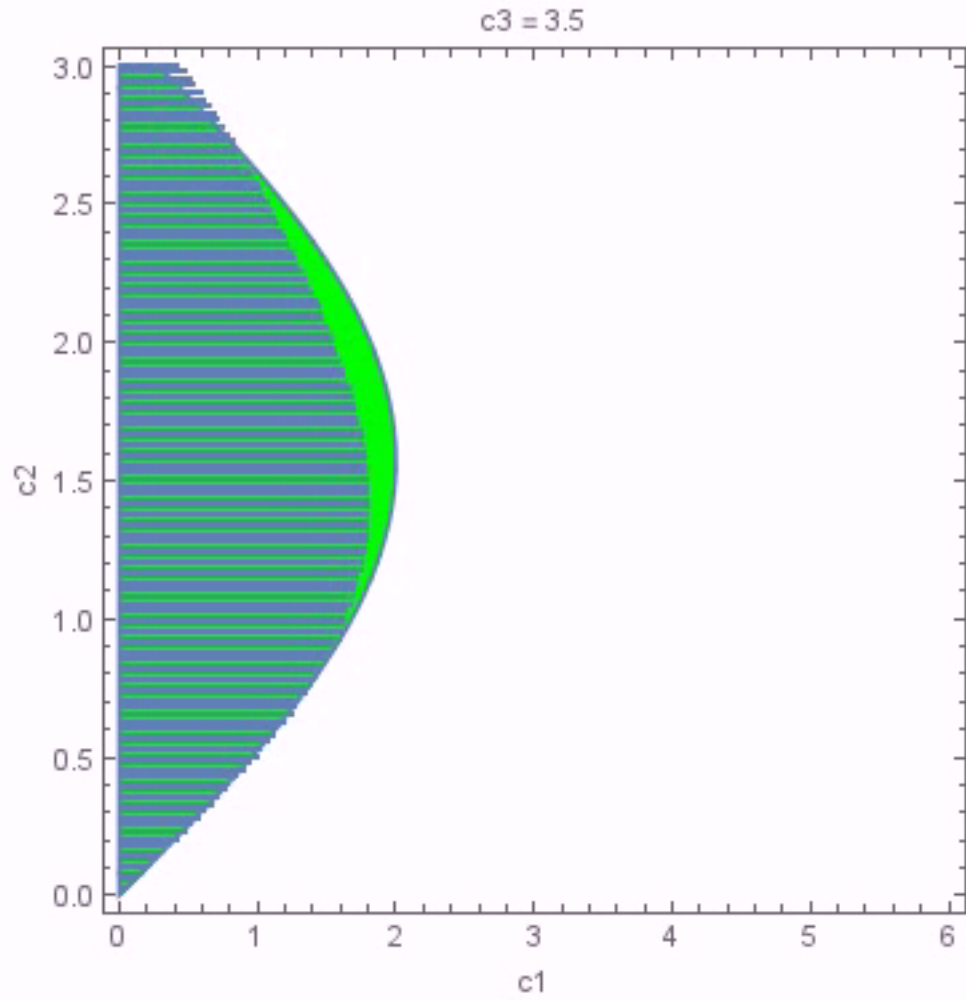


Figure 2.4: Region of parameter space which support entanglement harvesting which supports entanglement harvesting for $c_3 = 3.5$. The green region is calculated with the stationary phase approximation, while the region defined by blue dots is calculated numerically.

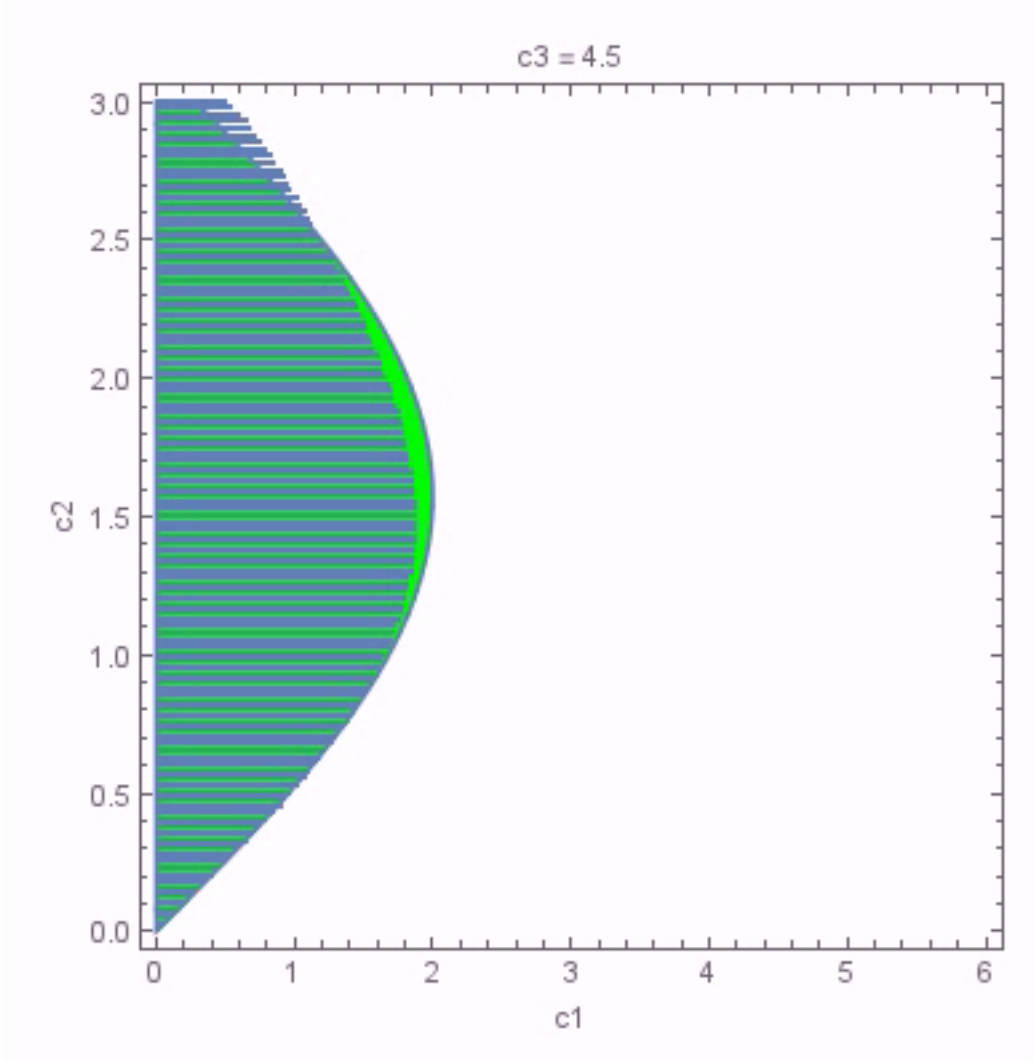


Figure 2.5: Region of parameter space which support entanglement harvesting which supports entanglement harvesting for $c_3 = 4.5$. The green region is calculated with the stationary phase approximation, while the region defined by blue dots is calculated numerically.

Chapter 3

Background about Cosmic Bubble

Collisions and Inflation

The boom and bust proposal[6] for inflation provides a mechanism for triggering the beginning of reheating which involves neither a flat potential energy function for the inflaton field nor super-Planckian field values. In preparation for my proposal for extending boom and bust inflation, I will review the motivation for and basics of the theory of inflation. I will also review the theory of compact extra dimensions and of the behavior of cosmic bubbles during collisions. Finally, I will discuss the discretization of the problem and the symplectic partitioned Runge-Kutta algorithm used to numerically simulate bubble collisions in Chapter 4.

3.1 Cosmological Inflation

The theory of inflation was first proposed by Guth[4] as a potential solution to the flatness, horizon, and monopole problems in cosmology. The flatness problem arises from the observation that today's universe has a total density value $\Omega_{\text{tot}} = 1.0023 \pm 0.006$ which is close to the critical value $\Omega_c = 1$ corresponding to a flat universe. In FRW models of cosmology this implies[34] that $\Omega_{\text{tot}}^{-1} - 1$ must have been smaller by a factor of roughly 10^{60} at the Big Bang, which is only true for unnaturally finely-tuned initial conditions with Ω_{tot} very close to 1. The horizon problem[35] is the fact that FRW models of the Big Bang cannot explain the observed homogeneity of the cosmic microwave background on length scales larger than the particle horizon (as calculated in the FRW model) at the time of recombination. Regions of the sky separated by more than about 2° were never in causal contact with one another in FRW models, and yet the cosmic microwave background temperature is homogeneous over the entire sky with $T_{\text{CMB}} = 2.725^\circ K$ with only very small deviations $\Delta T/T_{\text{CMB}} \ll 10^{-4}$. The monopole problem is that many extensions of the Standard Model predict the existence of many magnetic monopoles, yet they are so rare (assuming they exist at all) that one has never been observed experimentally[36].

According to the theory of inflation, FRW models do not incorporate the effects of a crucial period in the universe's history– the inflationary era, taking place between roughly 10^{-36} and 10^{-32} seconds after the Big Bang. During inflation, the universe expanded exponentially and non-adiabatically, driven by the energy density of a scalar inflaton field ϕ , so that $a(t) \sim e^{Ht}$ grew by a factor of roughly 10^{30} (about 70 e-

foldings) in total. This magnified previously microscopic length scales to cosmological length scales. The flatness problem is solved by observing that during periods of exponential expansion, $\Omega_{\text{tot}} - 1$ shrinks instead of growing, so that after inflation $\Omega_{\text{tot}} - 1 \sim 10^{-60}$ even if $\Omega_{\text{tot}} - 1 \sim 1$ prior to inflation. Consequently, the particle horizon for our universe is much larger than FRW theories predict—enough for all of the observable universe to have been in causal contact prior to inflation so that thermal equilibrium could be established. The monopole problem is solved by the observation that monopoles are produced at very high temperatures before inflation occurs but not afterwards. Even if monopoles were common before inflation, the rapid expansion will decrease the average magnetic monopole density of the universe so much that it is no surprise that none have ever been observed. At the end of inflation, energy is transferred from the inflaton field to conventional matter in a process known as reheating.

In Guth's original model, known as old inflation, inflation is driven by the energy density inflation field ϕ which initially takes on a constant value $\phi = \phi_F$ where ϕ_F is a minimum of the inflaton potential energy $V(\phi)$. The value $V(\phi_F)$ is only a local minimum of $V(\phi)$, but there is also a global minimum ϕ_V which can be reached via bubble nucleation. The universe expands exponentially, driven by the energy density $V(\phi_F)$. The hope was to have a model in which reheating is triggered by a first order phase transition as the inflaton quantum tunnels through the potential barrier into the basin of attraction of a new, lower minimum ϕ_V , creating bubbles of field with interior value ϕ_V which percolate throughout space. However, upon closer examination[37] it was found that old inflation cannot lead to percolation while also

explaining the homogeneity of the observable universe.

A fix to the theory of inflation was provided by "new inflation", proposed both by Linde[5] and by Albrecht and Steinhardt[38], in which inflation occurs as the inflaton ϕ slowly rolls down a hill of potential after the cooling of the universe changes the effective potential so that the original false vacuum value ϕ_F is no longer a minimum of the potential. Further investigation[39] of the proposal showed the possibility of eternal inflation, in which the inflationary phase lasts forever in most of the universe but ends locally inside of nucleated inflaton bubbles.

Consider an 3+1d FRW spacetime containing only a homogeneous scalar field. The dynamics of this system are governed by the equations

$$\ddot{\phi} + 3H\dot{\phi} = -V'(\phi) \tag{3.1}$$

$$H^2 = \frac{8\pi}{3M_{\text{pl}}^2} \left[\frac{1}{2}\dot{\phi}^2 + V(\phi) \right] \tag{3.2}$$

where $H = \dot{a}/a$ and $M_{\text{pl}} = G^{-1/2}$ is the Planck mass. The slow roll approximation is said to hold if $\frac{1}{2}\dot{\phi}^2 \ll V(\phi)$ and $\ddot{\phi} \ll 3H\dot{\phi}$. If the slow roll approximation holds, then $\dot{\phi} \approx -V'(\phi)/3H$ as ϕ moves towards a potential minimum. It can be shown that for slow roll inflation, the universe will expand by a factor of e^N where the number of e-foldings N is given by $N = \frac{8\pi}{M_{\text{pl}}^2} \int_{\phi_F}^{\phi_V} d\phi V(\phi)/V'(\phi)$. In order for this proposal to be consistent with observable data, $V(\phi)$ must be chosen with a flat region which is large enough for around 70 e-folds to take place. Reheating begins when ϕ reaches the potential minimum.

The boom and bust inflation proposal combines features of old and new inflation. As in old inflation, it is possible to choose the potential $V(\phi)$ generically without needing a flat region in which the slow roll approximation will be valid. Moreover, reheating is triggered by a collision of bubbles in the inflaton field. As in new inflation, our universe is inside of a single inflaton bubble. My extension to the boom and bust proposal will restrict the class of usable potentials to ones in which coherent bubble collisions are possible.

3.2 Nucleation and Collision of Cosmic Bubbles

The theory of bubble nucleation via quantum tunneling for scalar fields was explored in a seminal series[40][41][42] of papers by Coleman et al. as a field-theoretic extension of the theory of quantum tunneling of particles. In the case of a particle, the rate of tunneling through a potential barrier $V(q)$ can be calculated[43] in the path-integral formulation of quantum mechanics by finding instanton solutions to the classical equation of motion— that is, solutions to the classical equation of motion in Euclidean time which interpolate between a local potential minimum $V(q_F)$ located at $q = q_F$ when $\tau = -\infty$ and the tunneling point q_U outside the potential well for which $V(q_F) = V(q_U)$ when $\tau = 0$. The Euclidean equation of motion, $\ddot{q} = V'(q)$, is equivalent to the classical equation of motion for a particle in a potential $-V(q)$. The tunneling rate which is obtained from the WKB approximation can also be derived from the path integral formulation of quantum mechanics by summing over instantons.

A similar phenomenon occurs in field theory. Consider a scalar field ϕ on 3+1d

spacetime with a potential $V(\phi)$ which has two minima, again labeled ϕ_F and ϕ_V , satisfying $V(\phi_V) < V(\phi_F)$. Initially the field ϕ has a constant value ϕ_F . Coleman showed that in Euclidean time, there exists an $O(4)$ symmetric solution $\phi(s) = \phi(\sqrt{\tau^2 + \vec{x}^2})$ to the Euclidean equations of motion satisfying the equation

$$\phi''(s) + \frac{3}{s}\phi'(s) = V'(\phi(s)) \quad (3.3)$$

with boundary conditions $\phi(\infty) = \phi_F$ and $\phi'(0) = 0$. If the difference between the two potential minima $V(\phi_F)$ and $V(\phi_V)$ is small, then one can use the thin wall approximation

$$\phi''(s) = U'(\phi(s)) \quad (3.4)$$

where we assume that the potential $V(\phi)$ can be written as $V(\phi) = U(\phi) + \epsilon(\phi_V - \phi)/(\phi_V - \phi_F)$ for some small parameter ϵ and a potential energy function $U(\phi)$ which has degenerate minima located (neglecting shifts of order ϵ) at ϕ_F and ϕ_V . The form of the perturbation is chosen so that ϵ is the energy difference in potential minima after the degeneracy is broken. If the potential $V(\phi)$ had three or more approximately degenerate minima, there are instanton solutions interpolating between each consecutive pair of minima. Making use of the fact that ϕ' must vanish if $\phi = \phi_F$, this can be integrated to yield a first-order ODE

$$\phi'(s) = \sqrt{[2(U(\phi(s)) - U(\phi_F))]} \quad (3.5)$$

which determines the approximate shape of the bubble wall when combined with

the initial condition $\phi(R) = (\phi_F + \phi_V)/2$ which specifies that the middle of the bubble wall be located at $s = R$. The bubble radius is determined by minimizing the action of the instanton with respect to R , which in 3+1d yields $R = 3S_1/\epsilon$ where $S_1 = \int ds [\frac{1}{2}\phi'(s)^2 + U(\phi(s))]$.

Bubbles expand after nucleating, with the acceleration of the bubble walls driven by the potential energy difference between ϕ_F and ϕ_V . As a bubble expands, its walls become thinner via Lorentz contraction, approaching the limit of infinitely thin walls traveling at the speed of light.

If multiple bubbles nucleate, they may eventually collide as their walls expand depending on the rate of expansion of the space containing them. The behavior of the walls upon colliding has a complicated dependence both on the potential $V(\phi)$ and the speed of the walls at collision. For many potentials used to model inflation[44], the walls run through each other only to turn around and move towards one another to collide again. Each collision leads to the emission of radiation in the ϕ field, with the energy stored in the walls usually radiated away after only a few collisions. However, this is not the only possible result of a bubble collision.

Previous work[45][46] has established that in the case of ultrarelativistic wall collisions, the behavior of the walls immediately following the collision is described by the "free passage approximation." Given a collision between two bubbles of interior field value ϕ_V and exterior false vacuum value ϕ_F , the free passage approximation corresponds to the statement that for ultrarelativistic collisions between the bubbles the field in the collision region will be driven to the value $\phi_V - (\phi_F - \phi_V) = 2\phi_V - \phi_F$. If this value lies in the basin of attraction of a new potential minimum, it is possible[47]

to have a coherent transition to a new vacuum state in the collision region. It is also possible[48] that this process fails if the collision is not sufficiently ultrarelativistic.

3.3 Compact Extra Dimensions

Proposals for the existence of compact extra dimensions have a history dating back to Kaluza and Klein's suggestion[49] that 3+1d gravity and electromagnetism are both manifestations of 4+1d gravity on a spacetime with a compact 5th dimension. More recent proposals invoking extra dimensions include the ADD model[50], which uses an extra dimension to address the hierarchy problem, and string theory, which requires the existence of compact extra dimensions for consistency.

The existence of compact extra dimensions can be tested experimentally by looking for deviations from the inverse square law of Newtonian gravity. In a theory with n non-compact spatial dimensions, one expects to see a gravitational force $\propto 1/r^{n-1}$. With 3 noncompact dimensions and n compact extra dimensions of size d , gravity scales $\propto 1/r^{n+2}$ for $r \ll d$ and $\propto 1/r^2$ for $r \gg d$. Experiments[51] have placed an upper bound of $\sim 50\mu m$ on the diameter of a compact extra dimension.

In the boom and bust inflation proposal, a compact extra dimension allows a bubble in the inflaton field to trigger reheating via a self-collision after the bubble finishes wrapping around the extra dimension.

3.4 Discretization and the Symplectic Partitioned Runge-Kutta Algorithm

My extension of boom and bust inflation requires numerically solving the 1+1d partial differential equation of motion

$$\frac{\partial^2 \phi}{\partial t^2} - \frac{\partial^2 \phi}{\partial x^2} = -\frac{dV}{d\phi} \quad (3.6)$$

for the inflaton field ϕ for a given potential $V(\phi)$ and set of initial conditions. To compute the solution, I introduce a lattice discretization of the inflaton field so the problem can be modeled as a classical mechanical system with a large but finite number of degrees of freedom. I then apply a 4th-order symplectic partitioned Runge-Kutta algorithm to time-evolve the system.

Discretization

The equations governing the inflaton field can be derived from the action

$$S = \int dt \int dx \left[\frac{1}{2} \dot{\phi}^2 - \frac{1}{2} \left(\frac{\partial \phi}{\partial x} \right)^2 - V(\phi) \right] \quad (3.7)$$

To approximate this system by one with a finite number of degrees of freedom, I introduce a spatial grid on which the variables $\phi_n(t) = \phi(n\Delta x, t)$ are defined. Here $\Delta x = d/N$, where d is the circumference of the compact extra dimension and N is the number of gridpoints in the discretization. Approximating the spatial derivative

as $\frac{\partial\phi}{\partial x} = (\phi_{n+1} - \phi_n)/\Delta x$, the discretized system is governed by the action

$$S = \int dt \sum_{i=1}^N \left[\frac{1}{2} \dot{\phi}_i^2 - \frac{1}{2\Delta x^2} (\phi_i - \phi_{i-1})^2 - V(\phi_i) \right] \quad (3.8)$$

where we use the convention that $\phi_0 = \phi_N$. Converting to the Hamiltonian formalism and defining momentum variables $\pi_n = \dot{\phi}_n$ yields the Hamiltonian

$$H(\vec{\phi}, \vec{\pi}) = \sum_{i=1}^N \left[\frac{1}{2} \pi_i^2 + \frac{1}{2\Delta x^2} (\phi_i - \phi_{i-1})^2 + V(\phi_i) \right] \quad (3.9)$$

from which follow the equations of motion

$$\begin{aligned} \dot{\phi}_i &= \pi_i \\ \dot{\pi}_i &= \frac{1}{\Delta x^2} (\phi_{i+1} - 2\phi_i + \phi_{i-1}) - V'(\phi_i) \end{aligned} \quad (3.10)$$

for ϕ_i, π_i where $i = 1, \dots, N$.

Symplectic Partitioned Runge-Kutta

To discretize time with time-step Δt , I make use of a symplectic partitioned Runge-Kutta method[52]. Let ϕ_i^n and π_i^n be the numerically calculated values of ϕ_i and π_i at the time $n\Delta t$. The symplectic partitioned Runge-Kutta family of methods are specialized numerical algorithms used for dynamical systems whose equations of motion can be derived from a separable Hamiltonian $H(\vec{q}, \vec{p}) = T(\vec{p}) + V(\vec{q})$ for some set of position and momentum variables \vec{q} and \vec{p} .

One of the basic results regarding classical Hamiltonian mechanics is Liouville's

i	1	2	3	4	5	6
b_i	0.20725	0.41449	0.41449	0.41449	-0.12174	-0.65796
B_i	-0.12174	0.41449	0.41449	0.41449	0.20725	0.00000

Table 3.1: Coefficients b_i and B_i used in the 4th order symplectic partitioned Runge-Kutta method.

theorem that area is conserved under time-evolution in phase space. Symplectic integrators are constructed[53][54][55] so as to preserve this property when discretizing time, which guarantees approximate conservation of energy for exponentially long times. A symplectic partitioned Runge-Kutta method is a symplectic integrator which time-evolves the system using separate explicit Runge-Kutta methods for position and momentum variables. For an s -stage symplectic partitioned Runge-Kutta scheme, a single timestep over a time Δt starting from the state $\vec{\phi}_n = (\phi_1^n, \dots, \phi_N^n), \vec{\pi}_n = (\pi_1^n, \dots, \pi_N^n)$ is computed by setting $\vec{Q}_0 = \vec{\phi}, \vec{P}_1 = \vec{\pi}$, computing Q_1, \dots, Q_s and P_2, \dots, P_{s+1} using the equations

$$\vec{Q}_i = \vec{Q}_{i-1} + \Delta t B_i \vec{P}_i \quad (3.11)$$

$$\vec{P}_{i+1} = \vec{P}_i - \Delta t b_i V'(\vec{\phi}) \quad (3.12)$$

for some coefficients b_i and B_i , and finally setting $\vec{\phi}_{n+1} = Q_s, \vec{\pi}_{n+1} = P_{s+1}$. In the simulations discussed in this thesis, I use a scheme where $s = 6$ and which is 4th order in Δt . The coefficients, which correspond to the scheme used by Mathematica's internal implementation of 4th order symplectic partitioned Runge-Kutta, are given in Table 3.1. The time-step Δt is determined by Mathematica so as to obtain a

relative error smaller than 10^{-7} .

Chapter 4

Coherent Bubble Collisions in Boom and Bust Inflation

4.1 Introduction

The nucleation and collision of cosmic bubbles in the inflaton field ϕ provide a potential mechanism by which inflation can begin and end in the early universe [4]. Models of the universe which propose compact extra dimensions of space are also of independent interest.

One recent proposal for a graceful exit to inflation is given by boom and bust inflation [6]. In the boom and bust proposal, we consider inflation in a spacetime with compact extra dimension(s)– inflation begins when a bubble nucleates out of the false vacuum and starts to expand, and lasts until the expanding bubble collides with itself after having wrapped around the compact extra dimension(s). The self-collision of the bubble walls triggers the start of reheating as the collision leads to

the emission of radiation in the inflaton field.

The boom and bust proposal places a lower bound on the size d of a compact extra dimension via the requirement that inflation last long enough to expand the universe by a factor of roughly e^{70} before reheating begins. Brown derives a lower bound on d ,

$$d > R + 2H^{-1} \log \frac{2e^{70} H}{S(\text{reheating})^{1/2}} \quad (4.1)$$

where $S(\text{reheating})$ is the entropy density of the universe at the time of reheating. His argument assumes that reheating begins at a time approximately $d/2$ after the bubble nucleation when the self-collision of the bubble walls occurs. It should be noted that this neglects the impact of Hubble friction which slows down the expansion of the bubble wall. I will also neglect the impact of Hubble friction in my numerical simulation of bubble collisions. Hubble friction increases the amount of time before the bubble self-collision, so incorporating its effects should lead to an even smaller lower bound on the size of the compact extra dimension.

Observe that for some choices of inflaton potential, not all self-collisions of a cosmic bubble will lead to significant radiation emission and thus trigger reheating. For example, [47] noted that particular scalar potentials admit free passage field evolutions upon bubble collision, which can coherently drive the field to a new potential minimum within the collision region without significant emission of radiation. Such an evolution would seem to allow for a smaller lower bound on the radius of the extra dimension – if it takes a time of approximately $d/2$ for the bubble to traverse a com-

compact extra dimension of size d , then allowing for n coherent self-collisions which do not trigger reheating it takes a time $(n+1)d/2$ until the first self-collision which emits significant amounts of radiation and triggers reheating. The minimum d necessary for inflation to last a fixed amount of time thus shrinks by a factor of $n+1$. As [6] noted that, in his scenario, d was typically an order of magnitude larger than naturalness would suggest, reasonably small values of n have the potential to address this issue.

I investigate the mechanics of this extended boom-and-bust inflation, taking account of the free passage coherent dynamics for a few specific choices of potentials. The ones we tested for which our proposal is successful have multiple minima which are spaced at approximately equal intervals. This is consistent with previous work on the free passage approximation for collision of ultrarelativistic solitons, according to which the collision of two bubbles with interior field value ϕ_t and external false vacuum field value $\phi_f > \phi_t$ drives the field in the collision region to the value $\phi_c = \phi_t - (\phi_f - \phi_t) = 2\phi_t - \phi_f$ immediately after the collision.

Following Brown's proposal, I focus on the limiting case $d \gg H^{-1}$ in which the expansion of the universe stretches the bubble along the non-compact directions so rapidly that the bubble's expansion and self-collision around the compact extra dimension can be approximated as a 1+1d domain wall collision. I examine radiation production in three families of potentials and show the possibility of coherent bubble collisions in the boom-and-bust scenario.

4.2 Basic Set-Up

Getting the Initial Conditions

I follow the discussion of bubble nucleation in Coleman [40], modified to account for the extra compact dimension of spacetime. Assume that we have a scalar field ϕ defined on our spacetime manifold \mathcal{M} , which we take to be the 4+1 dimensional manifold $\mathcal{M} = \mathcal{M}_4 \times S^1$ where \mathcal{M}_4 is 3+1 dimensional Minkowski space and S^1 is the circle of radius $d/2\pi$. The metric $\eta^{\mu\nu}$ is the usual Minkowski metric for 4 + 1 dimensions, but the compactness of the extra dimension manifests itself in the requirement that x_4 coordinate be periodic so that $\phi(t, \vec{x}, x_4 - d/2) = \phi(t, \vec{x}, x_4 + d/2)$. Take the potential energy $V(\phi)$ to be of the form

$$V(\phi) = U(\phi) + \epsilon \left(\frac{\phi_t - \phi}{\phi_t - \phi_f} \right) \quad (4.2)$$

where $U(\phi)$ has at least two degenerate minima whose locations we label by ϕ_f^0 and ϕ_t^0 for (unperturbed) false and true vacua, respectively. The dynamics of a scalar field on \mathcal{M} follow from the classical action

$$S = \int d^5x [\eta^{\mu\nu} \partial_\mu \phi \partial_\nu \phi - V(\phi)] \quad (4.3)$$

leading to the classical equation of motion

$$\frac{\partial^2 \phi}{\partial t^2} - \nabla^2 \phi = -V'(\phi) \quad (4.4)$$

I examine the bubble nucleation process by which a field starting in a false vacuum of constant value $\phi = \phi_f$ (and so, constant energy density $V(\phi_f)$) nucleates a bubble of field whose interior field value is ϕ_t . Assume that $R \ll d$, where R is the radius of the nucleated bubble, so that one may approximate the bubble profile after nucleation as being the same as it would be in 4+1d Minkowski space. Following the theory of quantum tunneling through barriers, the field tunnels through the classically forbidden region along a path which minimizes the barrier penetration coefficient B [40] [56]. This path corresponds to a "bounce" solution to the Euclidean equations of motion

$$\frac{\partial^2 \phi}{\partial \tau^2} + \nabla^2 \phi = V'(\phi) \quad (4.5)$$

(we have Wick rotated to imaginary time $\tau = it$) which we solve using an ansatz $\phi(s)$ in which the solution is $O(5)$ invariant. Defining $s = \sqrt{\tau^2 + x_1^2 + x_2^2 + x_3^2 + x_4^2}$ and letting ϕ be a function $\phi(s)$ of s , the equation of motion reduces to the ordinary differential equation

$$\phi'' + \frac{4}{s}\phi' = V'(\phi) \quad (4.6)$$

We work in the thin wall approximation for which $\epsilon \ll 1$, making the minima of $V(\phi)$ nearly degenerate. In the thin wall approximation the $\frac{4}{s}\phi'$ term can be neglected, as can the difference between $V(\phi)$ and $U(\phi)$, yielding (as in the 3+1d case discussed in Chapter 3)

$$\phi'' = U'(\phi) \quad (4.7)$$

which can be integrated (noting that we should have $\phi' = 0$ in the false vacuum $\phi = \phi_f$ to fix the constant of integration) to obtain

$$\phi' = \pm \sqrt{2(U(\phi) - U(\phi_f))} \quad (4.8)$$

Our choice of sign \pm for the square root determines whether the false vacuum ϕ_f will be located at $\pm\infty$. We solve this differential equation for $\phi(s)$ using the initial condition $\phi(R) = (\phi_t^0 + \phi_f^0)/2$ so that the wall $\phi(s)$ is centered halfway between the two minima at the bubble radius location R . The bubble radius is derived by minimizing the Euclidean action of the instanton with respect to R . Following Weinberg [56] but using four spatial dimensions, we find that the radius R which minimizes the Euclidean action is given by

$$R = 4\sigma/\epsilon \quad (4.9)$$

where

$$\sigma = \int_{-\infty}^{\infty} dx \left[\frac{1}{2} \phi'^2 + U(\phi) - U(\phi_f) \right] = \int_{\phi_t}^{\phi_f} d\phi \sqrt{2(U(\phi) - U(\phi_f))} \quad (4.10)$$

From this bounce solution, we obtain the initial conditions for the classical equations of motion which apply following the bubble nucleation. In particular,

$$\phi(0, x_1, x_2, x_3, x_4) = \phi \left(\sqrt{x_1^2 + x_2^2 + x_3^2 + x_4^2} \right) \quad (4.11)$$

$$\frac{\partial \phi}{\partial t}(0, x_1, x_2, x_3, x_4) = 0 \quad (4.12)$$

We assume that the rapid expansion of the universe immediately stretches the bubble along the non-compact directions, so that the bubble evolution can be approximated as a domain wall collision along the compact extra dimension. We also account for the perturbation to the potential by a slight shifting and scaling of the unperturbed wall function so that it interpolates between the minima of the perturbed potential.

$$\frac{\partial^2 \phi}{\partial t^2} - \frac{\partial^2 \phi}{\partial x_4^2} = V'(\phi) \quad (4.13)$$

with initial conditions

$$\phi(0, x_4) = \frac{\phi_f - \phi_t}{2} + \frac{\phi_f - \phi_t}{\phi_f^0 - \phi_t^0} \left[\phi(|x_4|) - \frac{\phi_f^0 + \phi_t^0}{2} \right] \quad (4.14)$$

$$\frac{\partial \phi}{\partial t}(0, x_4) = 0 \quad (4.15)$$

and periodic boundary condition

$$\phi(t, d/2) = \phi(t, -d/2) \quad (4.16)$$

The initial conditions are compatible with the requirement that ϕ be periodic with period d in x_4 because $\phi(0, d/2) = \phi(0, -d/2) = \phi(d/2) \approx \phi_f$. Note here that the absolute value $|x_4|$ ensures we have generated two walls located at $x_4 = \pm R$.

Bubble Expansion and Collision

Qualitatively speaking, as time goes forward the true vacuum region grows, wrapping around the compact dimension in both directions until the two walls collide. Lorentz invariance tells us that the full solution $\phi(t, x_4)$ in an uncompactified space will grow so as to have a radius $R(t) = \sqrt{R^2 + t^2}$ [56]. The same behavior occurs in the compactified case until the walls collide when $R(t) = d/2$ at time $t = \sqrt{d^2 - 4R^2}/2$ having reached a velocity of $v = \sqrt{1 - 4(R/d)^2}$. The previously imposed condition $R \ll d$ implies that the collision is ultrarelativistic.

Upon collision, the walls (considered as deviations from the false vacuum ϕ_f) approximately superimpose with one another to create a collision region whose field takes on the value ϕ_c . In the free passage approximation for ultrarelativistic collisions, this superposition is exact immediately following the collision. From here, the behavior of the field depends upon the behavior of the potential near ϕ_c .

For generic potentials we find that ϕ_c is not a minimum of $V(\phi)$, so the potential pushes the field in the collision region towards the potential minimum in whose basin of attraction ϕ_c is located. The field rolls down towards this minimum with some energy lost to radiation at the edges of the collision region. If there are no further wall collisions affecting this collision region, the field will eventually settle into the new minimum with the extra potential energy all radiated away. In the context of inflationary cosmology, the emission of this radiation triggers the beginning of reheating and the end of inflation. With a compactified extra dimension, there are certain to be additional wall collisions affecting the collision region— either the walls

will wrap around the extra dimension until they collide again or they will slow down, turn around, and collide again at the original collision point.

However, there are some choices of potential for which the collision need not lead to significant radiation production. For example, the sine Gordon equation corresponding to the potential $V(\phi) = 1 - \cos \phi$ is known to be integrable, leading to soliton collisions in which no radiation is produced at all. (Note that in the case of the exact sine Gordon equation, the potential minima are exactly degenerate— the bubble walls must be given nonzero initial velocities in order to move rather than being pushed outward by the potential energy difference between the bubble interior and exterior). More generally, we expect from the free passage approximation that a coherent transition will occur if the collision of two ultrarelativistic solitons drives the field in the collision region to a new potential minimum.

We choose three potential energy functions for which we analyze radiation created in bubble wall collisions. Soliton collisions for the unperturbed ($\epsilon = 0$) versions of each these collisions have been studied previously.

Two Minima Potential $U_1(\phi)$

Let

$$U_1(\phi) = \lambda(\phi^2 - \phi_0^2)^2 \tag{4.17}$$

We nondimensionalize by choosing $\hbar = c = \phi_0 = 1$, yielding

$$U_1(\phi) = \lambda(\phi^2 - 1)^2 \tag{4.18}$$

The minima of $U_1(\phi)$ are located at $\phi = \pm 1$. The unperturbed wall shape with $\phi(-\infty) = -1$ and $\phi(\infty) = 1$ is given by

$$\phi(s) = \tanh\left(\sqrt{2\lambda}s\right) \quad (4.19)$$

The perturbed minima are located at $\phi = \pm 1 + \epsilon/16\lambda$ to first order in ϵ . The one-dimensional action $\sigma = 4\sqrt{2\lambda}/3$, which implies the radius of the bubble is given by $R = 16\sqrt{2\lambda}/3\epsilon$.

Soliton collisions for unperturbed versions of this potential have been explored extensively. In the unperturbed case there is a rich phenomenology of possible outcomes of a collision. A wall collision can result in the walls passing through one another and heading off to infinity (in an uncompactified space), but it can also result in the walls turning around and colliding with each other again at least once— which possibility occurs depends in a complicated way on the velocity of the walls at the time of the collision. Exotic bound states such as bions can be formed as well [57]. All of these collisions give rise to radiation, though the amount varies with the velocity at collision.

Three Minima Potential $U_2(\phi)$

Let

$$U_2(\phi) = \lambda\phi^2(\phi^2 - \phi_0^2)^2 \quad (4.20)$$

Again, we pick $\phi_0 = 1$, yielding

$$U_2(\phi) = \lambda\phi^2(\phi^2 - 1)^2 \quad (4.21)$$

The minima of $U_2(\phi)$ are located at $\phi = 0, \pm 1$. The unperturbed wall shape with $\phi(-\infty) = \pm 1$ and $\phi(\infty) = 0$ is given by

$$\phi(s) = \pm \frac{1}{\sqrt{1 + 3e^{2\sqrt{2}\lambda s}}} \quad (4.22)$$

The perturbed minima are located at $\phi = \pm 1 + \epsilon/8\lambda, \epsilon/2\lambda$ to first order in ϵ . The one-dimensional action $\sigma = \frac{\sqrt{\lambda}}{2\sqrt{2}}$ yields the radius $R = \frac{\sqrt{2\lambda}}{\epsilon}$.

Kink-antikink collisions to the unperturbed version of this potential have been explored previously [58]. In addition, this potential has been explored in the context of collision-induced classical transitions and the free passage approximation [45] [47].

Perturbed sine Gordon $U_3(\phi)$

Let

$$U_3(\phi) = \lambda(1 - \cos \phi/\phi_0) \quad (4.23)$$

Again picking $\phi_0 = 1$, we get

$$U_3(\phi) = \lambda(1 - \cos \phi) \quad (4.24)$$

The minima of $U_3(\phi)$ are located at $\phi = 2\pi n$ for integer n . The unperturbed wall shape with $\phi(-\infty) = 0$ and $\phi(\infty) = 2\pi$ (all other wall shapes can be found by shifting by $2\pi n$) is given by

$$\phi(s) = 4 \tan^{-1} e^{\sqrt{\lambda}s} \quad (4.25)$$

The perturbed minima are located at $\phi = \sin^{-1}(\epsilon/2\pi\lambda) + 2\pi n = \epsilon/2\pi\lambda + 2\pi n$ to first order in ϵ . The one-dimensional action $\sigma = 8\sqrt{\lambda}$ yields a radius $R = \frac{32\sqrt{\lambda}}{\epsilon}$.

Both the perturbed and unperturbed versions of this potential have been widely discussed in the literature as the sine Gordon and perturbed sine Gordon models.

4.3 Numerical Evaluation

I used Wolfram Mathematica to explore numerical solutions to the equations of motion for each potential. I discretized space as discussed in Chapter 3, and then made use of the "NDSolve" routine within Mathematica to solve the 1+1d equation of motion with a fourth-order symplectic partitioned Runge-Kutta method. I simulated the behavior of bubble wall collisions for the three potential families discussed. For each choice of parameters, I show the evolution of the walls including a zoomed-in view of the regions near the walls where radiation is emitted upon wall collision. Within the zoomed-in views, the amplitude of the fluctuations is indicated by marking the locations of the vacuum field value at which the amplitude of deviations from the vacuum value reach 1% of a characteristic field value ϕ_c given by the value of ϕ at the first potential minimum whose unperturbed value is positive. I interpret the presence of fluctuations whose amplitude exceeds this value as a criterion for the beginning of

reheating.

For some choices of potential and d , the walls develop high-frequency low-amplitude fluctuations even before the walls begin to collide. These arise from spatial discretization error if the wall becomes too thin compared to the length scale of discretization. Their effect can be minimized by choosing parameters so that the collision occurs before the Lorentz contracted wall experiences significant discretization error.

I also choose values of d which are of the same order of magnitude as R to illustrate that a coherent transition can take place even if the $d/R \sim 1$. For larger values of d/R the speed of the walls at collision increases, increasing the validity of the free passage approximation of a coherent transition. This also improves the numerical quality of results – for ultrarelativistic speeds, the walls are length-contracted to be very thin which amplifies the effects of numerical discretization.

The numerical solutions are seen to conserve energy to within 0.01%, providing a degree of confidence in the accuracy of the results.

Two Minima Potential $V_1(\phi)$

Both examples used a spatial discretization with $N = 2000$ gridpoints.

First Example

Choose the nondimensionalized parameters $d = 90, \lambda = 0.8, \epsilon = 0.2$, which imply $R = 33.73$. As seen in Figure 4.1, the walls collide at $t \approx 17$. The field in the collision region is kicked towards the value $\phi \approx -3$ implied by the free passage approximation, but then is driven back towards the false vacuum value at $\phi \approx 1$ by the potential and

oscillates around this value, which leads to radiation emitted into the interior of the bubble. Zooming in on the bubble interior in Figure 4.2, we see radiation emitted by the collision travelling into the bubble interior starting at around $t \approx 26$. A new vacuum region does not nucleate and the radiation emitted by the first collision is larger than the 1% threshold. The energy distribution of the field is shown in Figure 4.3, and the presence of radiation can be seen from the oscillatory behavior following the first collision.

Second Example

We choose the nondimensionalized parameters $d = 200, \lambda = 1.0, \epsilon = 0.1$, which imply $R = 75.42$. The results are qualitatively similar to the first example. As seen in Figure 4.4, the walls collide at $t \approx 35$. The field in the collision region is kicked towards the value $\phi \approx -3$ implied by the free passage approximation, but then is driven back towards the false vacuum value at $\phi \approx 1$ by the potential and oscillates around this value, which leads to radiation emitted into the interior of the bubble. Zooming in on the bubble interior in Figure 4.5, we see radiation emitted by the collision travelling into the bubble interior starting at around $t \approx 60$. Again, a new vacuum region does not form and there is significant radiation emitted which is visible from the energy distribution graph Figure 4.6.

Three Minima Potential $V_2(\phi)$

Both examples used a spatial discretization with $N = 1000$ gridpoints.

First Example

Choose the nondimensionalized parameters $d = 80, \lambda = 1.0, \epsilon = 0.05$, which imply $R = 28.28$. As seen in Figure 4.7, the walls collide at $t \approx 17$. The field in the collision region is kicked towards the value $\phi \approx 1$ implied by the free passage approximation, which corresponds to the approximate location of another potential minimum. The walls continue moving through each other to loop back around the bubble until they collide again at $t \approx 59$, with radiation forming inside the collision region after the first collision but not leaking into the bubble interior until after the second. In Figure 4.8 we zoom in on the field near the middle vacuum value $\phi \approx 0$ to see that the interior region of the bubble remains approximately radiation-free after the collision, with fluctuations remaining less than 1% of the vacuum field value. In contrast Figure 4.9 shows the presence of significant radiation in the collision region around the vacuum field value $\phi \approx 1$. The energy distribution graph Figure 4.10 reveals that collisions can be detected by sudden spikes in the kinetic and stretch energies and that oscillatory behavior only becomes visible after the second collision.

Second Example

Choose the nondimensionalized parameters $d = 60, \lambda = 0.5, \epsilon = 0.05$, which imply $R = 20.00$. As seen in Figure 4.11, the walls collide at $t \approx 13$. The field in the collision region is kicked towards the value $\phi \approx 1$ implied by the free passage approximation, which corresponds to the approximate location of another potential minimum. The walls continue moving through each other to loop back around the bubble until they

collide again at $t \approx 44$, with radiation forming inside the collision region after the collision but not leaking into the bubble interior. In Figure 4.12 we zoom in on the field near the middle vacuum value $\phi \approx 0$ to see that the interior region of the bubble remains approximately radiation-free after the collision, with fluctuations remaining less than 1% of the vacuum field value. However, the fluctuations are noticeably larger than those in the previous example. In contrast Figure 4.13 shows the presence of significant radiation in the collision region around the vacuum field value $\phi \approx 1$. The energy distribution graph Figure 4.14 again reveals that the second collision generates much more radiation than the first.

Sine-Gordon Potential $V_3(\phi)$

Both examples used a spatial discretization with $N = 2500$ gridpoints.

First Example

Choose the nondimensionalized parameters $d = 130, \lambda = 0.447, \epsilon = 0.428$, which imply $R = 49.99$. As seen in Figure 4.15, the walls first collide at $t \approx 22$, passing through each other and creating small amounts of radiation in the collision region and bubble interior. They collide again at time $t \approx 90$ with both the interior and exterior regions remaining below the 1% minimum threshold criterion. Figure 4.16 shows fluctuations around vacuum corresponding to the bubble interior during and after the first wall collision. It is seen that only a small amount of radiation is created by the collision. Figure 4.17 shows fluctuations about the vacuum of the collision region before and after the second wall collision. Note that the fluctuations are

larger than in Figure 4.16, but are still below the 1% threshold. Figure 4.18 shows the fluctuations produced after a third wall collision, which have now reached the 1% threshold. The energy distribution graph Figure 4.19 reveals signs of significant radiation only following the third collision.

Second Example

Choose the nondimensionalized parameters $d = 800, \lambda = 1.0, \epsilon = 0.1$, which imply $R = 320.00$. As seen in Figure 4.20, the walls first collide at $t \approx 130$, passing through each other but with a buildup of fluctuations near the bubble wall in the collision region. The bubble interior seen in Figure 4.21 does not contain significant amounts of radiation, but the collision region seen in Figure 4.22 does contain high-frequency oscillations which exceed the 1% threshold. These are likely due to spatial discretization error. The energy distribution graph Figure 4.23 contains oscillatory behavior starting at $t \approx 220$.

4.4 Discussion

Theoretical arguments and numerical data suggest it is possible to delay the onset of reheating in the boom and bust inflation model until the first non-coherent self-collision of the bubble walls. In the case of the two minimum potential $V_1(\phi)$, emission of radiation begins shortly before the collision of the walls. In the case of the potential $V_2(\phi)$ with three minima, it is possible for the first self-collision to create a new vacuum region, though with the emission of some amount of radiation. In the case of

the perturbed sine Gordon potential $V_3(\phi)$, it is possible to have many self-collisions which each create a new vacuum region, with only small amounts of radiation emitted in the first few collisions.

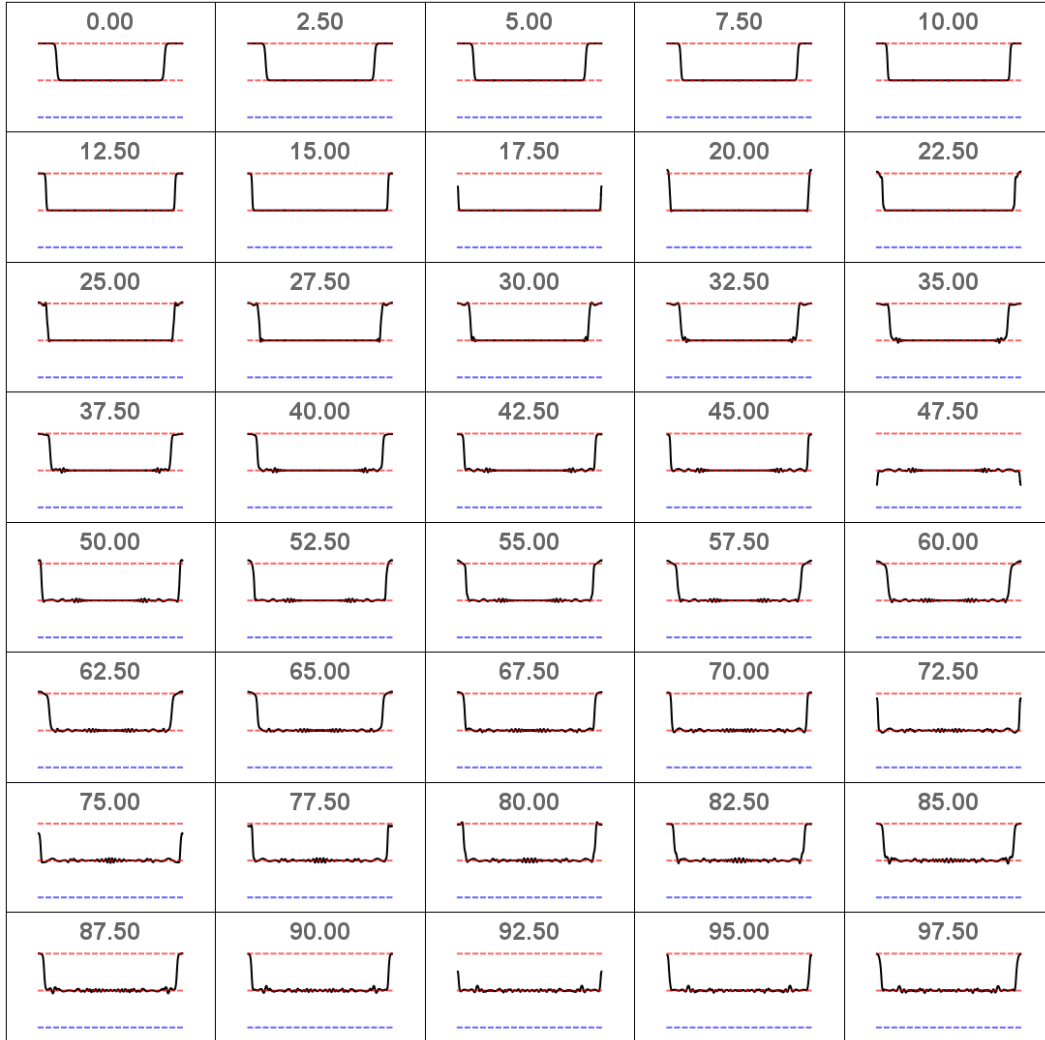


Figure 4.1: Evolution of the bubble for the first example of the two-minimum potential. The red lines are the potential minima at $\phi \approx \pm 1$, and the blue line is the value $\phi \approx -3$ to which the field is kicked in the free passage approximation.

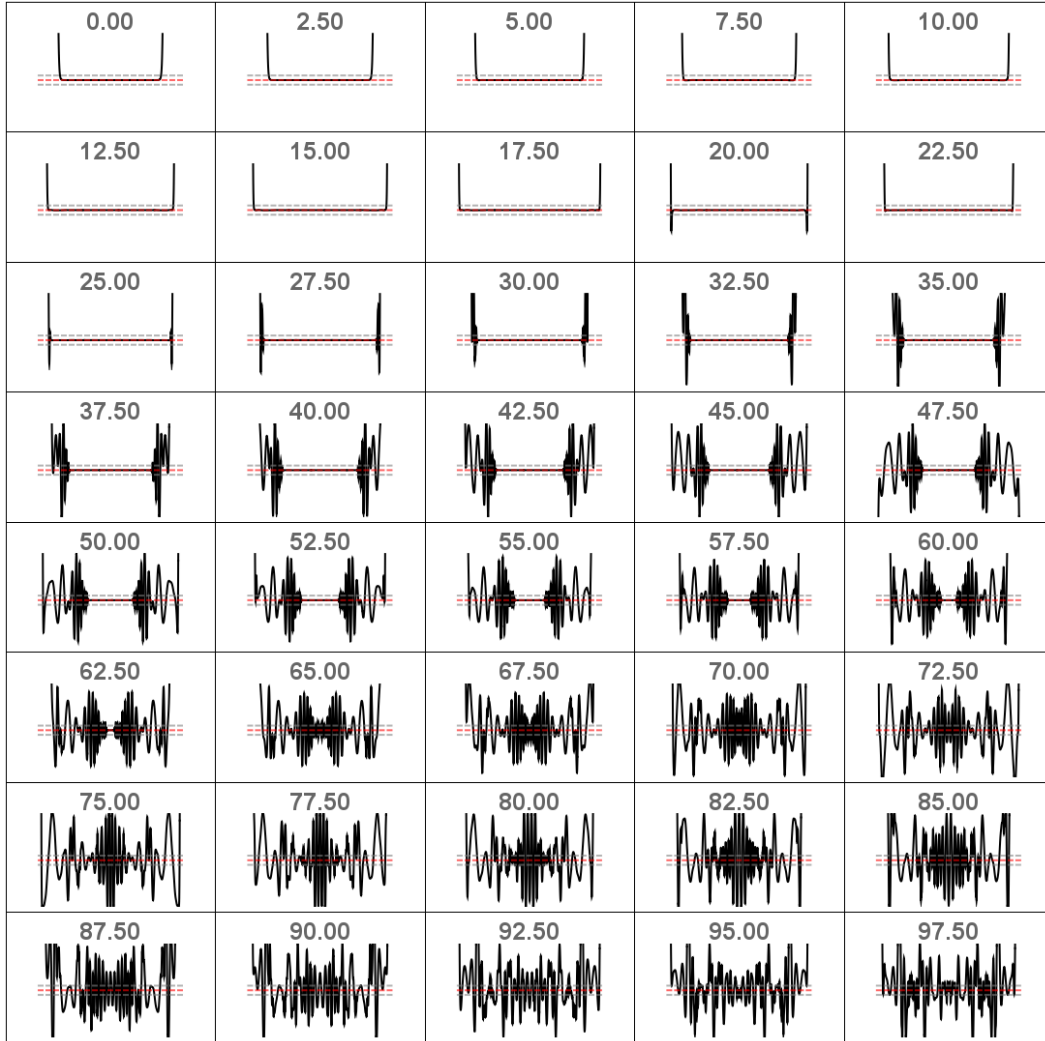


Figure 4.2: Radiation formation around inside the bubble near the wall for the first example of the two-minimum potential. The red line is the vacuum field value, and the gray lines correspond to deviations from this value by 1% of the magnitude of the vacuum field value $\phi \approx 1$.

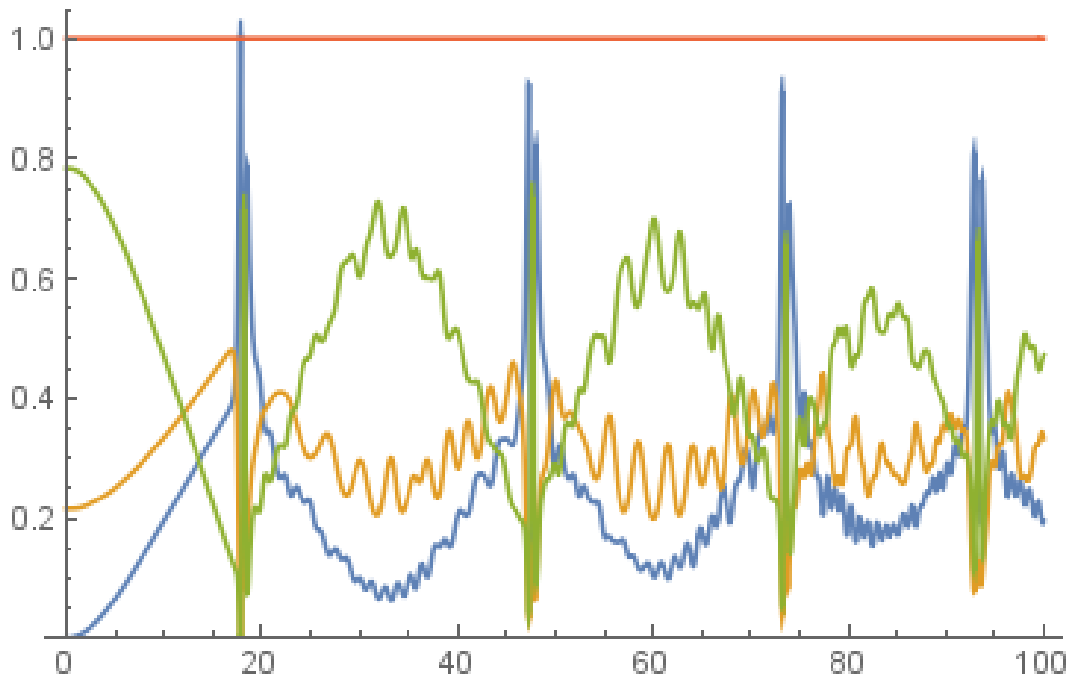


Figure 4.3: Energy distribution in the first example of the two-minimum potential. Blue represents kinetic energy, yellow represents the stretch potential energy $\frac{1}{2} \left(\frac{\partial \phi}{\partial x} \right)^2$, and green represents potential energy due to $V(\phi)$, all normalized so that total energy (red) is 1. The x-axis depicts time.

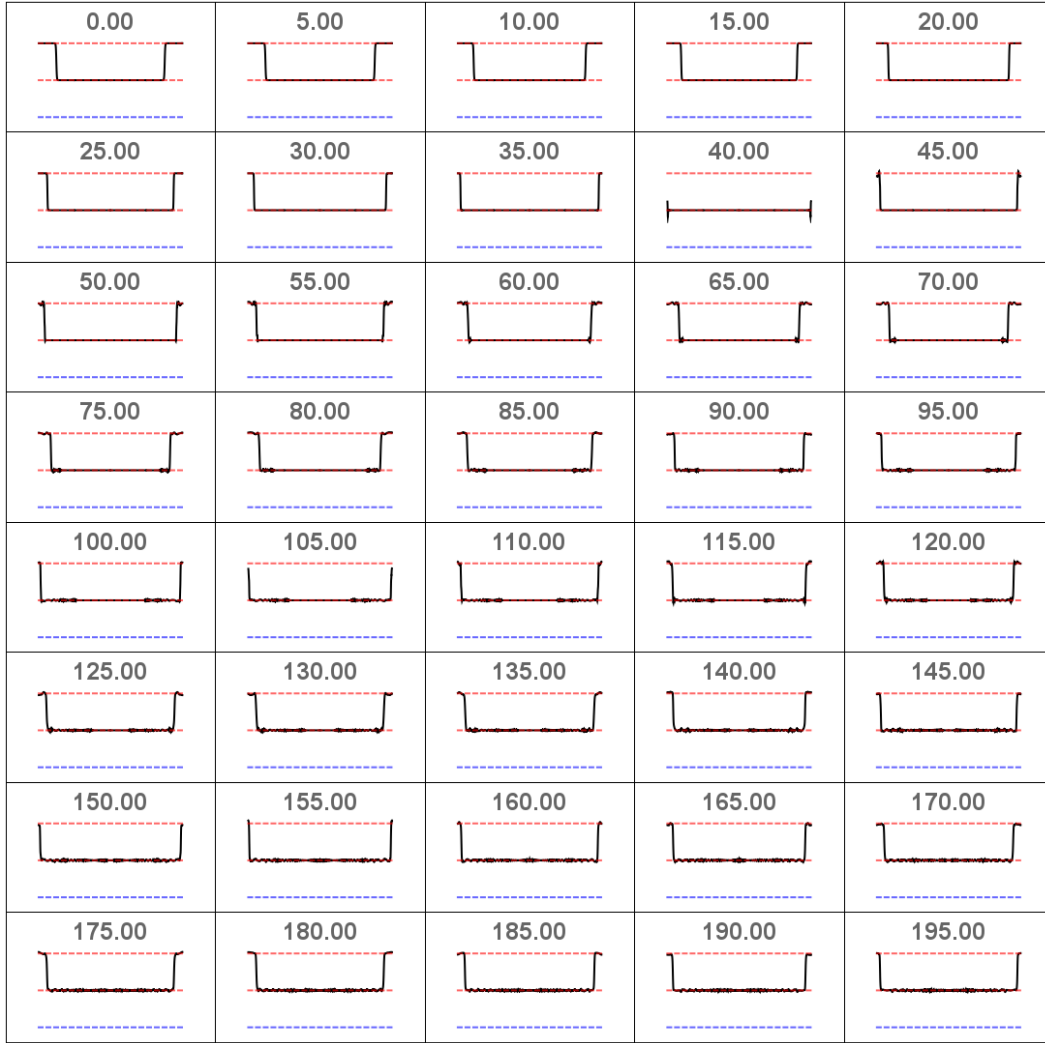


Figure 4.4: Evolution of the bubble for the second example of the two-minimum potential. The red lines are the potential minima at $\phi \approx \pm 1$, and the blue line is the value $\phi \approx -3$ to which the field is kicked in the free passage approximation.

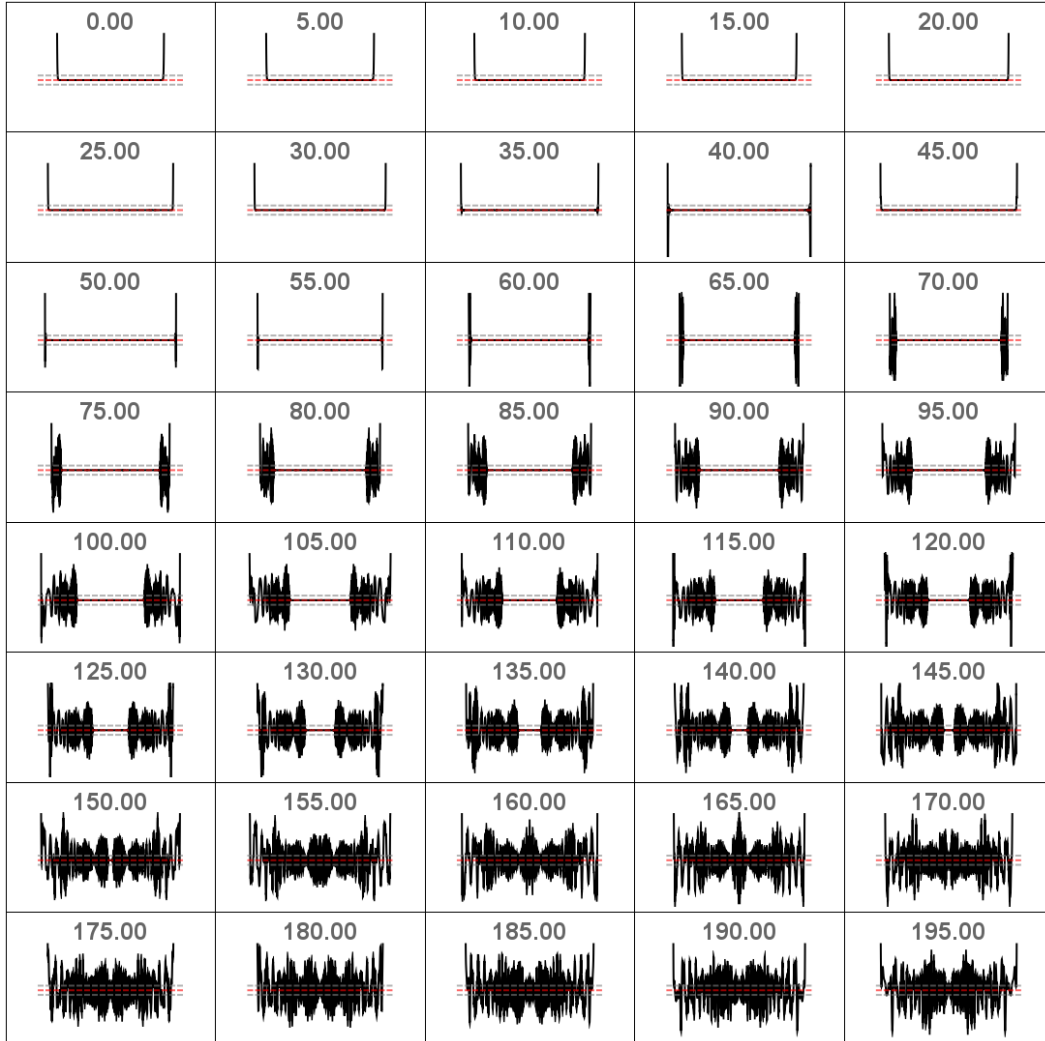


Figure 4.5: Radiation formation around inside the bubble near the wall for the second example of the two-minimum potential. The red line is the vacuum field value, and the gray lines correspond to deviations from this value by 1% of the magnitude of the vacuum field value $\phi \approx 1$.

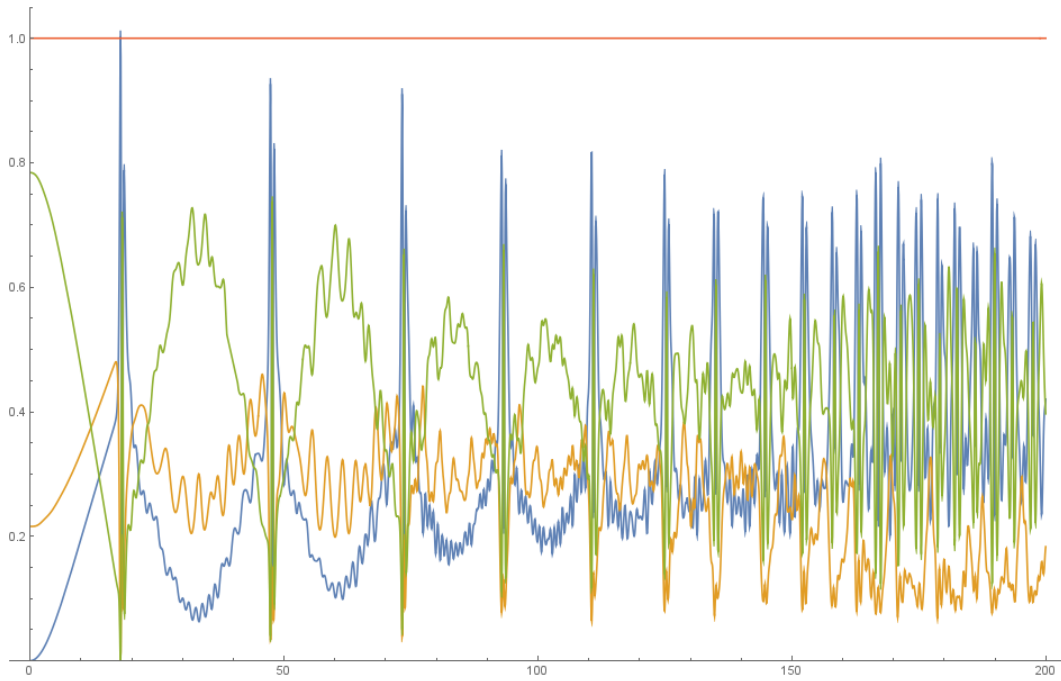


Figure 4.6: Energy distribution in the second example of the two-minimum potential. Blue represents kinetic energy, yellow represents the stretch potential energy $\frac{1}{2} \left(\frac{\partial \phi}{\partial x} \right)^2$, and green represents potential energy due to $V(\phi)$, all normalized so that total energy (red) is 1. The x-axis depicts time.

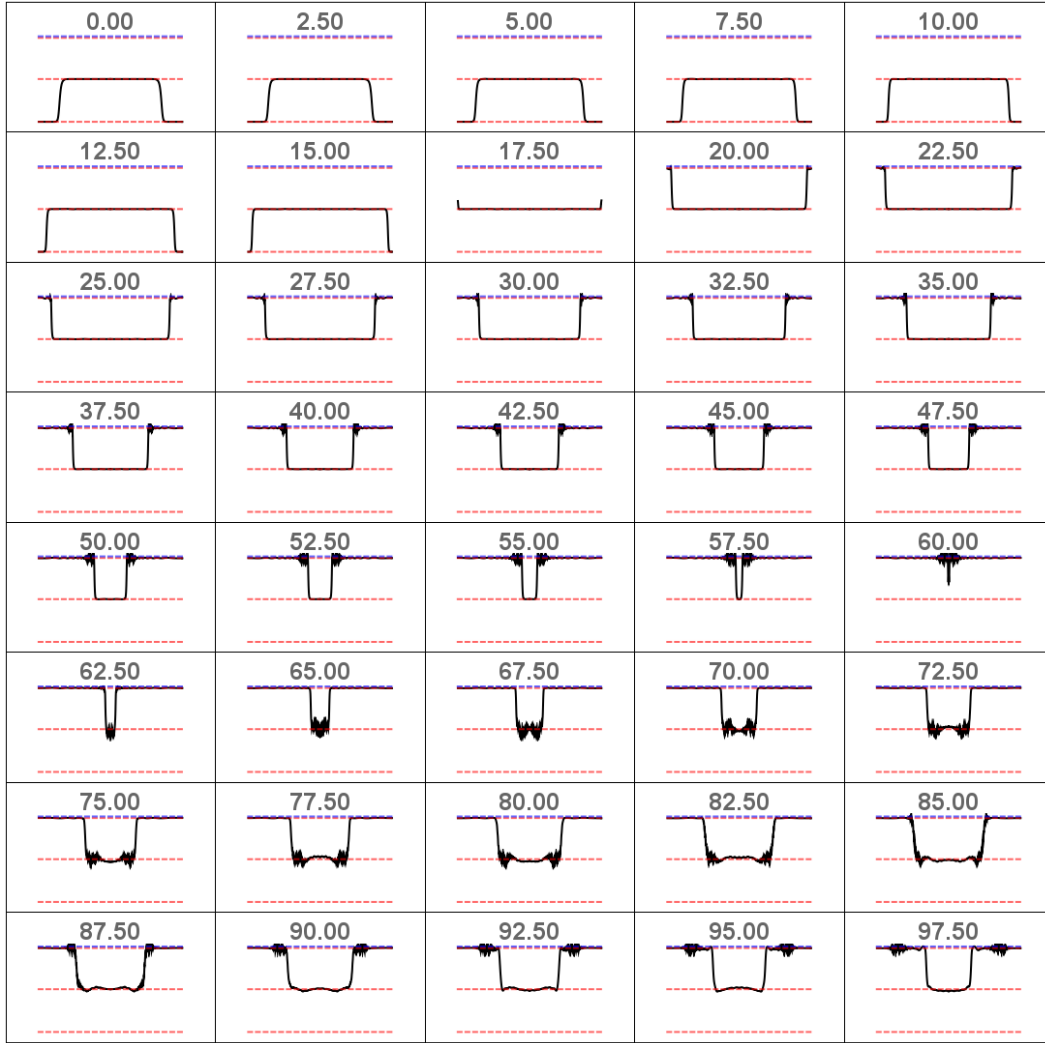


Figure 4.7: Evolution of the bubble for the first example of the three-minimum potential. The red lines are the potential minima at $\phi \approx 0, \pm 1$, and the blue line is the value $\phi \approx 1$ to which the field is kicked in the free passage approximation.

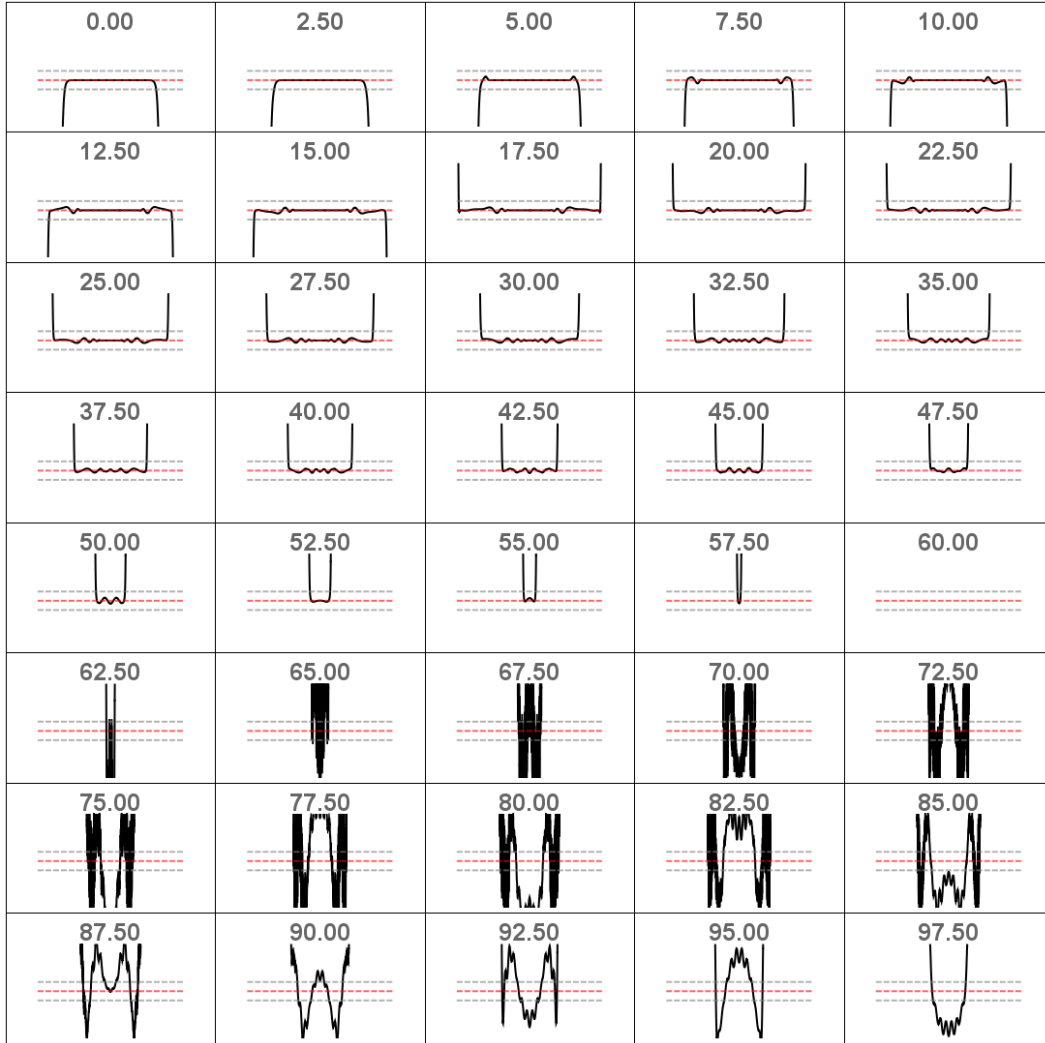


Figure 4.8: Zooming in on middle vacuum $\phi \approx 0$ near the walls in the bubble interior after the first collision in the first example of the three-minimum potential. The field inside the bubble remains well within the 1% threshold until the second collision.

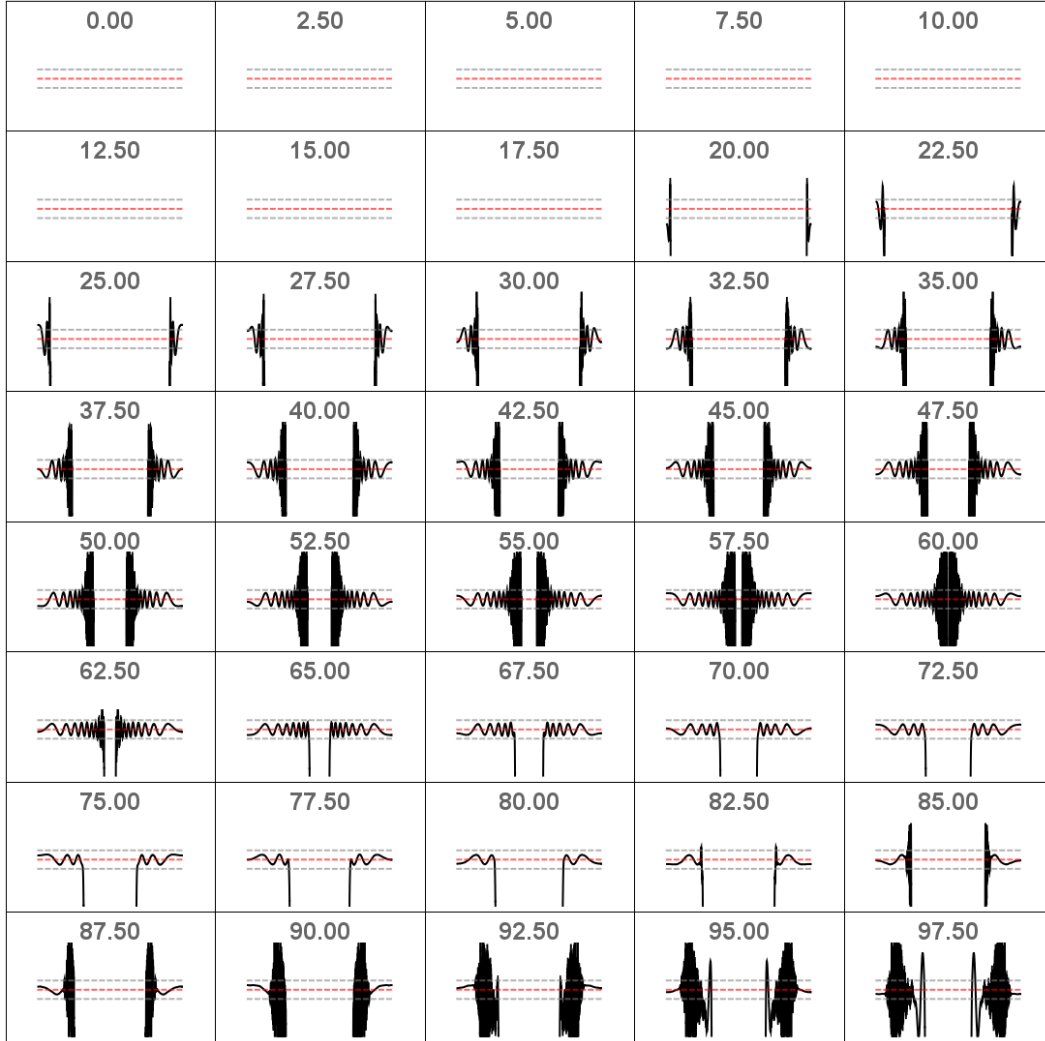


Figure 4.9: Zooming in on top vacuum $\phi \approx 1$ near the walls in the collision region after the first collision in the first example of the three-minimum potential. The field in this region develops radiation which exceeds the 1% threshold, but which does not propagate into the bubble interior.

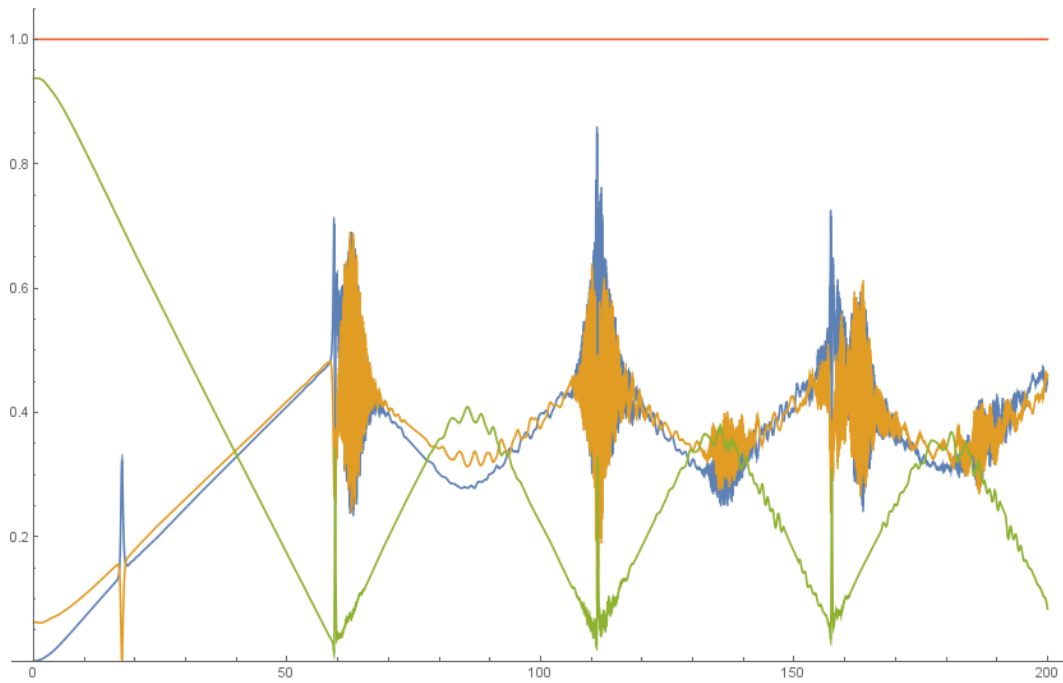


Figure 4.10: Energy distribution in the first example of the three-minimum potential. Blue represents kinetic energy, yellow represents the stretch potential energy $\frac{1}{2} \left(\frac{\partial \phi}{\partial x} \right)^2$, and green represents potential energy due to $V(\phi)$, all normalized so that total energy (red) is 1. The x-axis depicts time.

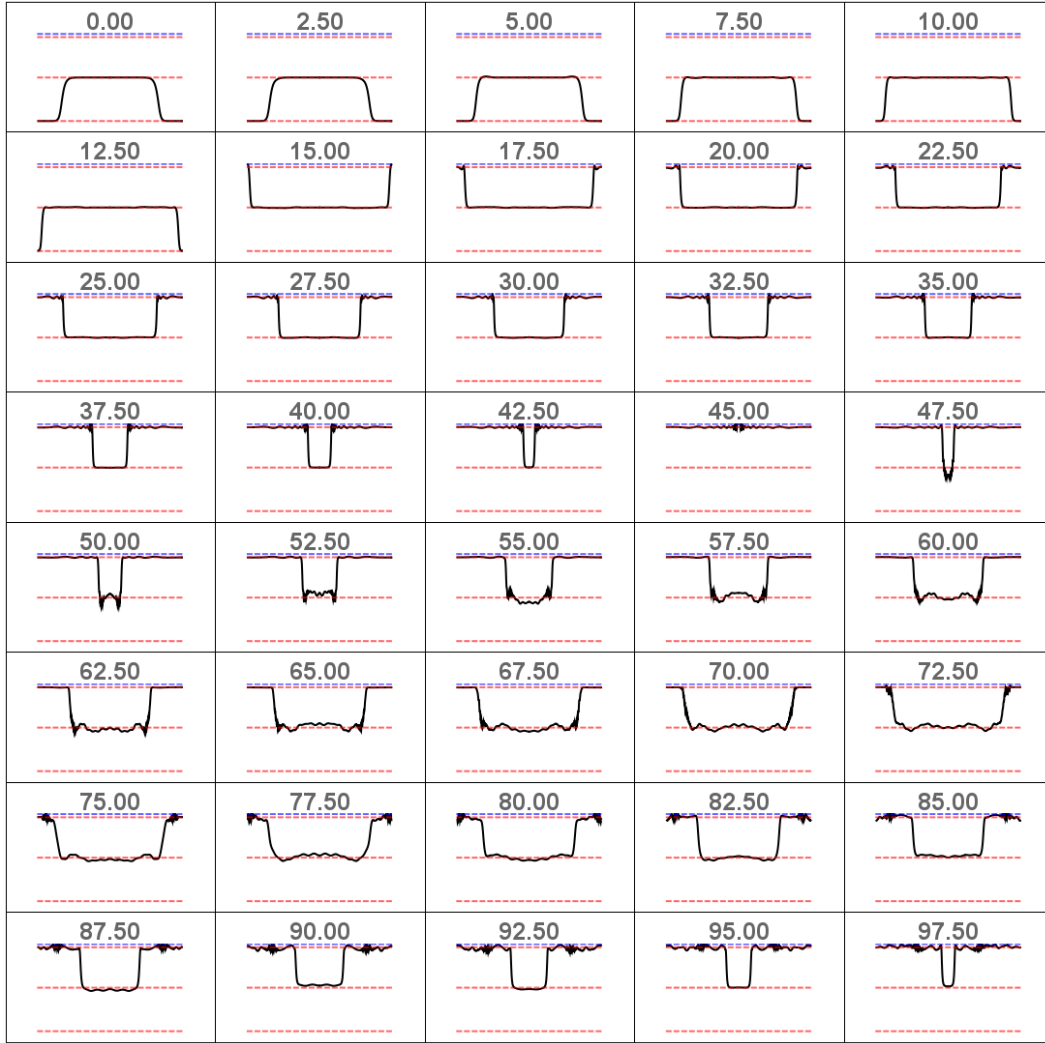


Figure 4.11: Evolution of the bubble for the second example of the three-minimum potential. The red lines are the potential minima at $\phi \approx 0, \pm 1$, and the blue line is the value $\phi \approx 1$ to which the field is kicked in the free passage approximation.

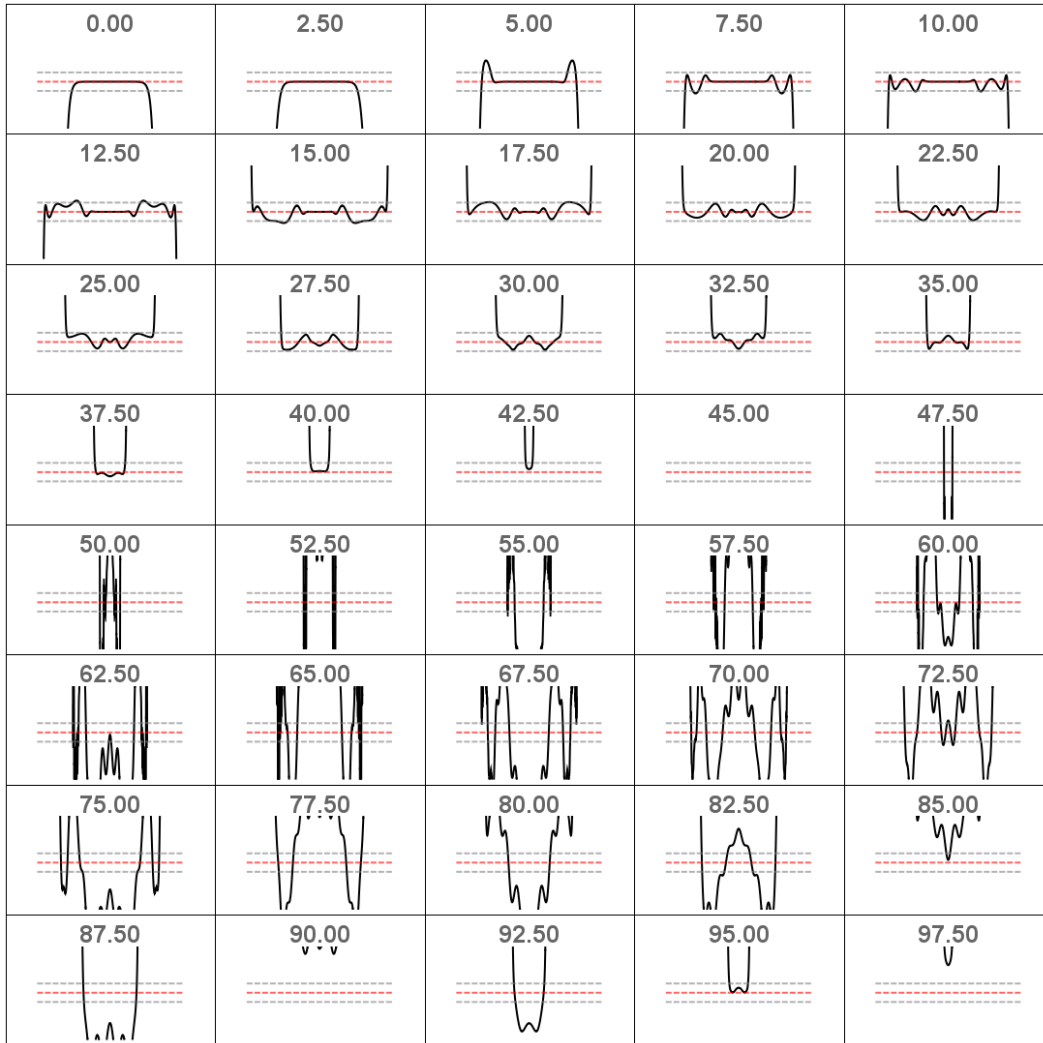


Figure 4.12: Zooming in on middle vacuum $\phi \approx 0$ near the walls in the bubble interior after the first collision in the second example of the three-minimum potential. The field inside the bubble remain at around 1% threshold until the second collision.

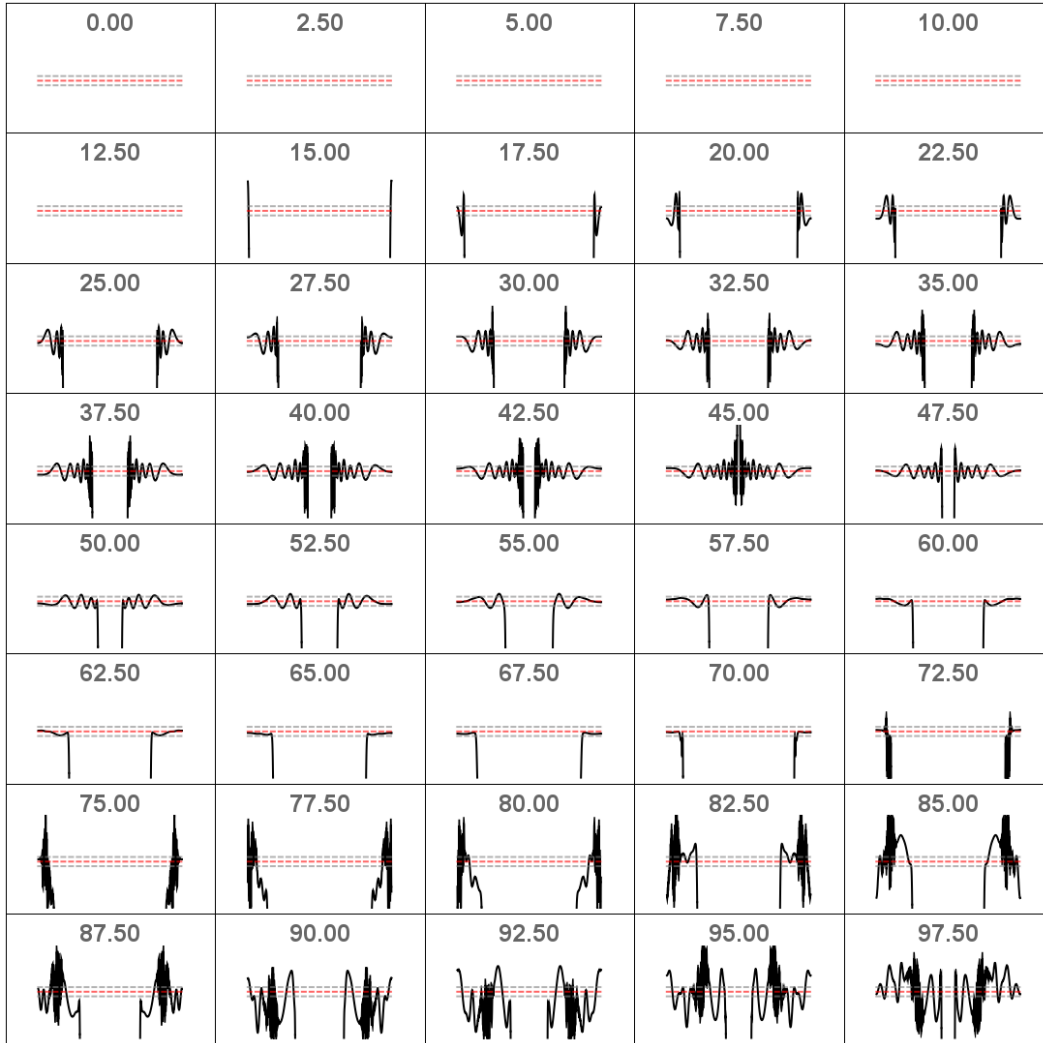


Figure 4.13: Zooming in on top vacuum $\phi \approx 1$ near the walls in the collision region after the first collision in the second example of the three-minimum potential. The field in this region develops radiation which exceeds the 1% threshold, but which does not propagate into the bubble interior.

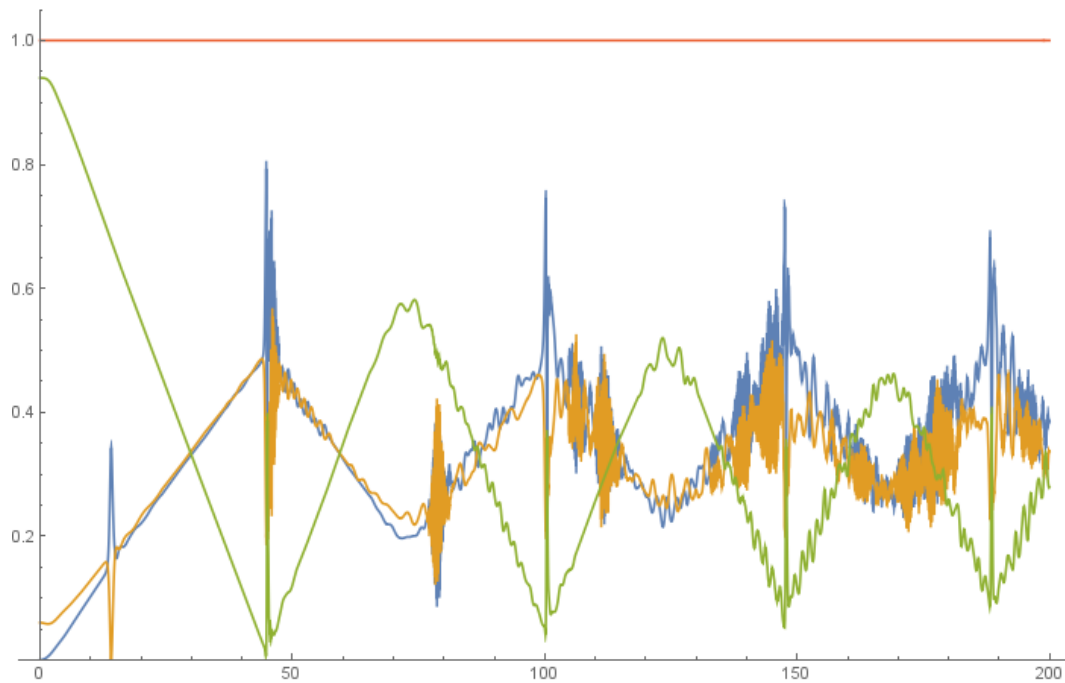


Figure 4.14: Energy distribution in the second example of the three-minimum potential. Blue represents kinetic energy, yellow represents the stretch potential energy $\frac{1}{2} \left(\frac{\partial \phi}{\partial x} \right)^2$, and green represents potential energy due to $V(\phi)$, all normalized so that total energy (red) is 1. The x-axis depicts time.



Figure 4.15: Evolution of the bubble for the first example of the sine-Gordon potential. The red lines are the potential minima at $\phi \approx 2\pi n$ for integer n , and the blue line is the value $\phi \approx 4\pi$ to which the field is kicked in the free passage approximation after the first collision.

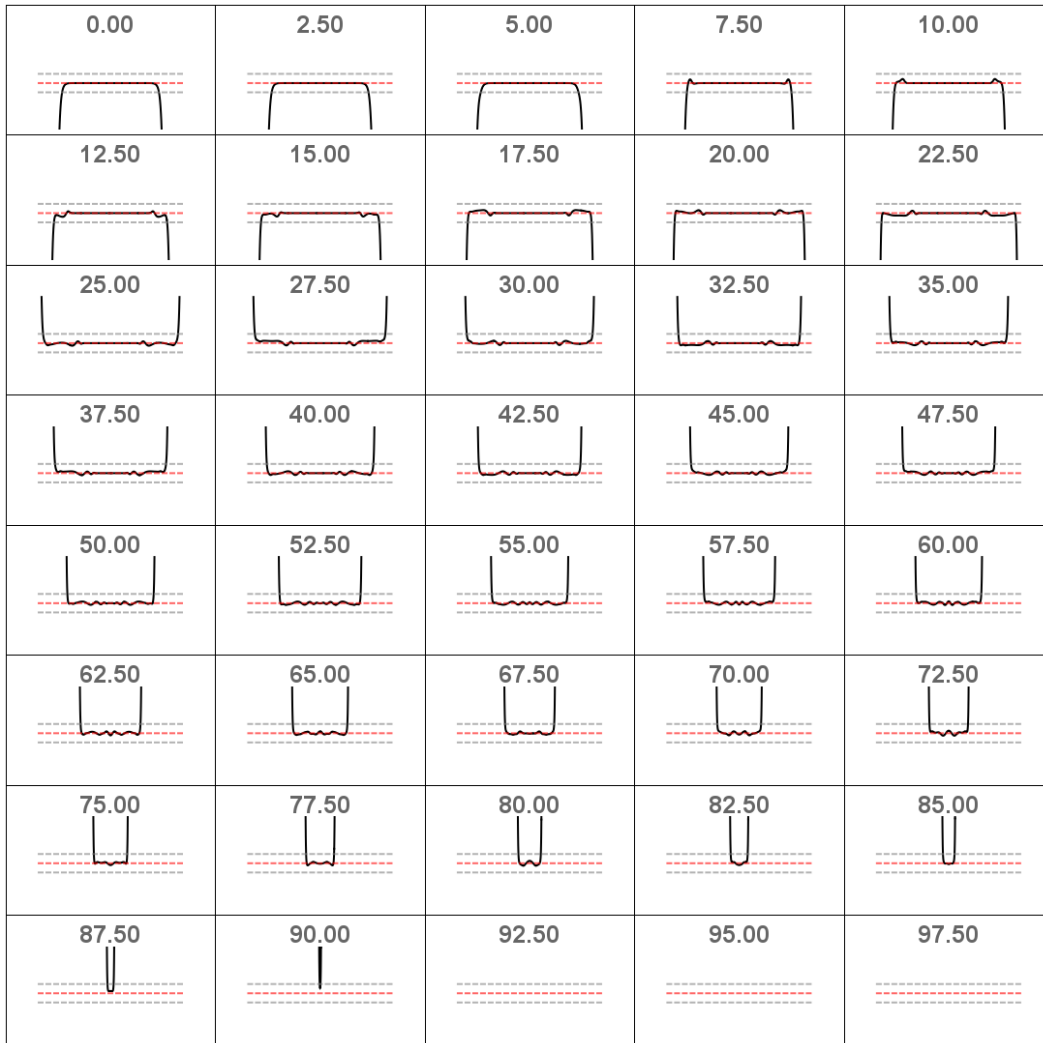


Figure 4.16: Zooming in on original bubble interior $\phi \approx 2\pi$ near the walls in the bubble interior after the first collision in the first example of the sine-Gordon potential. The field inside the bubble remains well below the 1% threshold until the second collision.

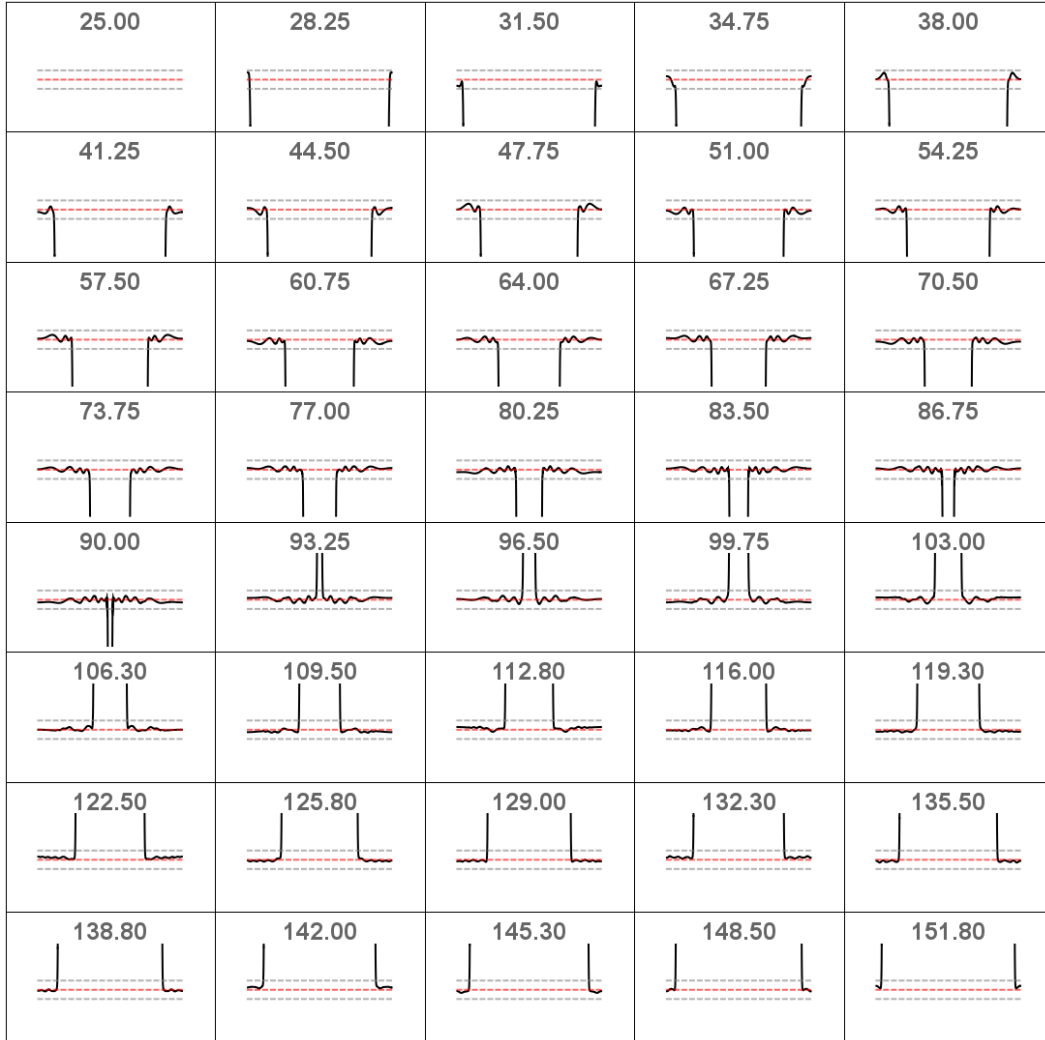


Figure 4.17: Zooming in on first collision region vacuum value $\phi \approx 4\pi$ after the first collision in the first example of the sine-Gordon potential. The field inside the collision region has radiation of amplitude well below the 1% threshold level.

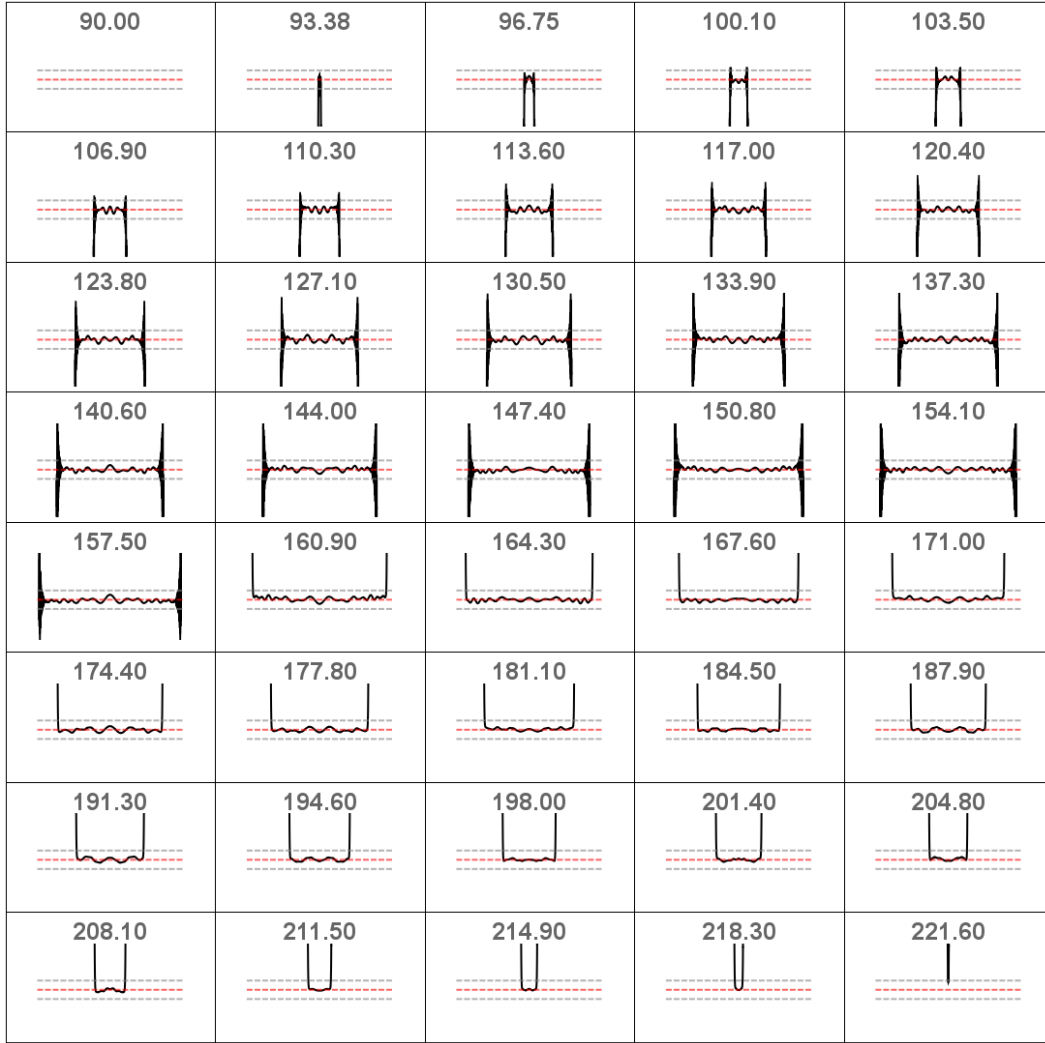


Figure 4.18: Zooming in on second collision region vacuum value $\phi \approx 6\pi$ after the second collision in the first example of the sine-Gordon potential. The field inside the collision region has radiation of amplitude well below 1% threshold level.

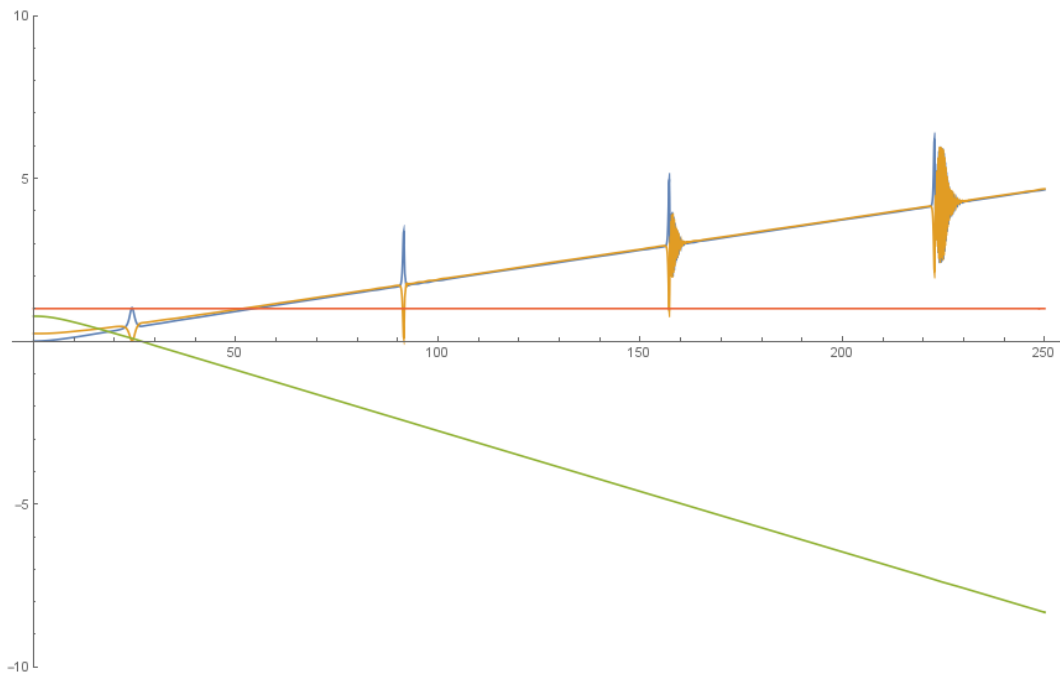


Figure 4.19: Energy distribution in the first example of the sine-Gordon potential. Blue represents kinetic energy, yellow represents the stretch potential energy $\frac{1}{2} \left(\frac{\partial \phi}{\partial x} \right)^2$, and green represents potential energy due to $V(\phi)$, all normalized so that total energy (red) is 1. The x-axis depicts time.

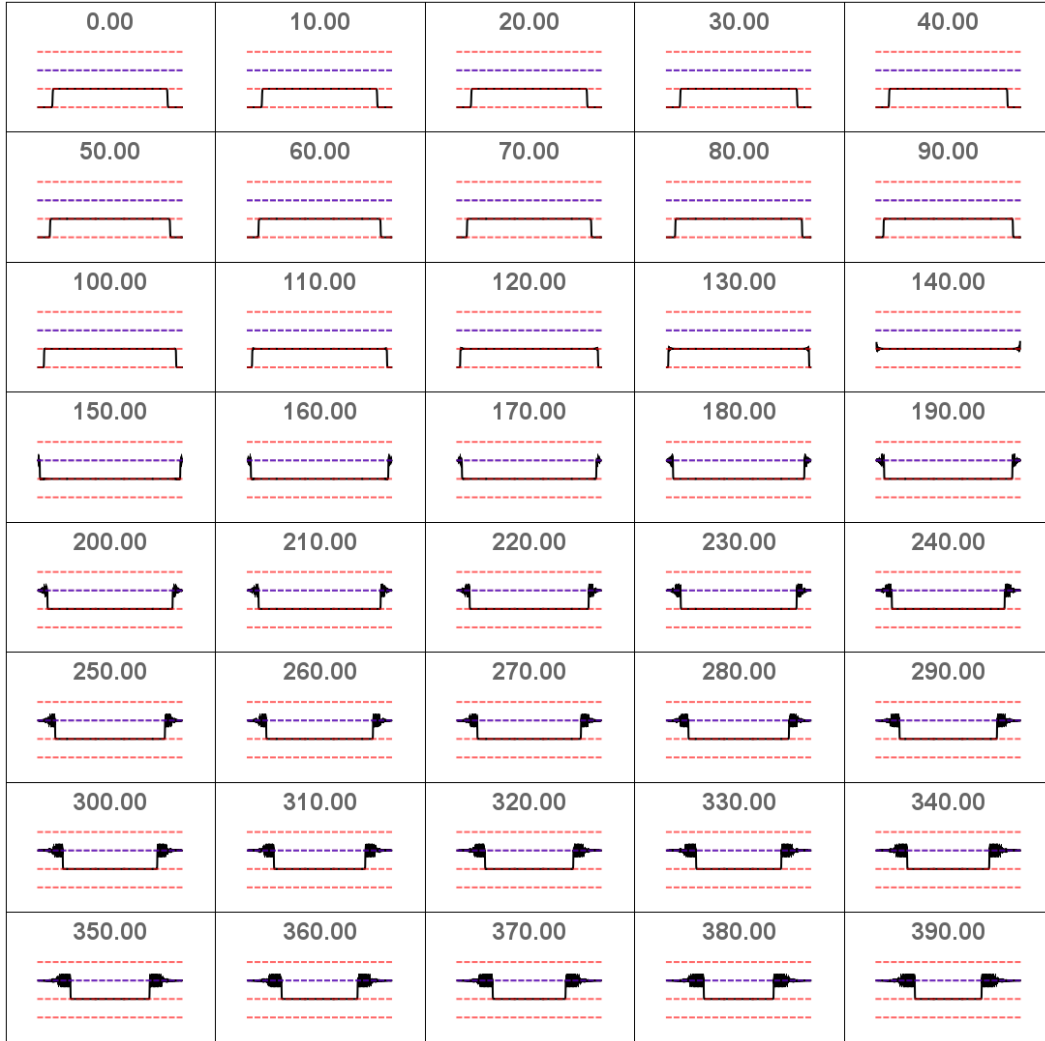


Figure 4.20: Evolution of the bubble for the second example of the sine-Gordon potential. The red lines are the potential minima at $\phi \approx 2\pi n$ for integer n , and the blue line is the value $\phi \approx 4\pi$ to which the field is kicked in the free passage approximation after the first collision.

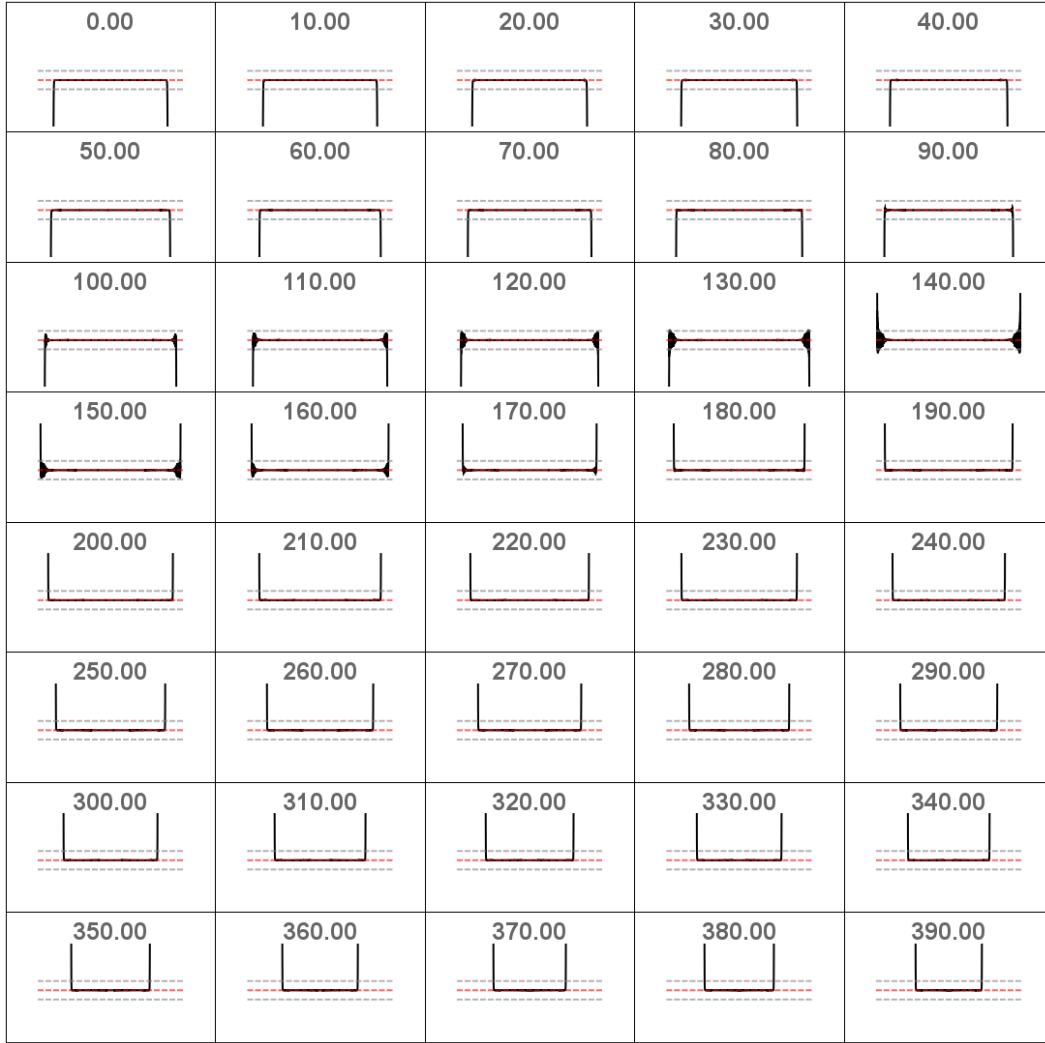


Figure 4.21: Zooming in on original bubble interior $\phi \approx 2\pi$ near the walls in the bubble interior after the first collision in the second example of the sine-Gordon potential. The field inside the bubble remains well within the 1% threshold.

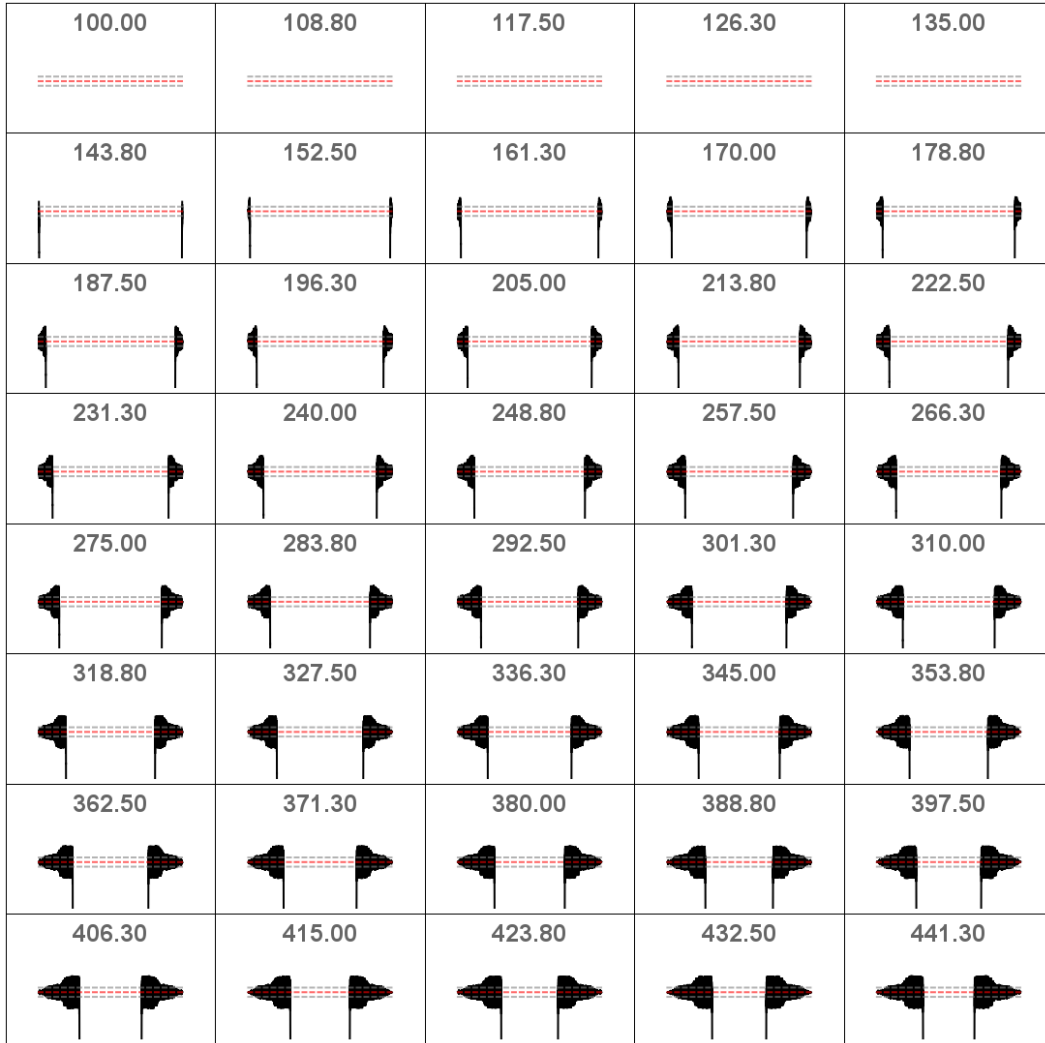


Figure 4.22: Zooming in on first collision region vacuum value $\phi \approx 4\pi$ after the first collision in the second example of the sine-Gordon potential. The field inside the collision region has high frequency oscillations concentrated near the bubble wall, which are likely to be caused by spatial discretization error.

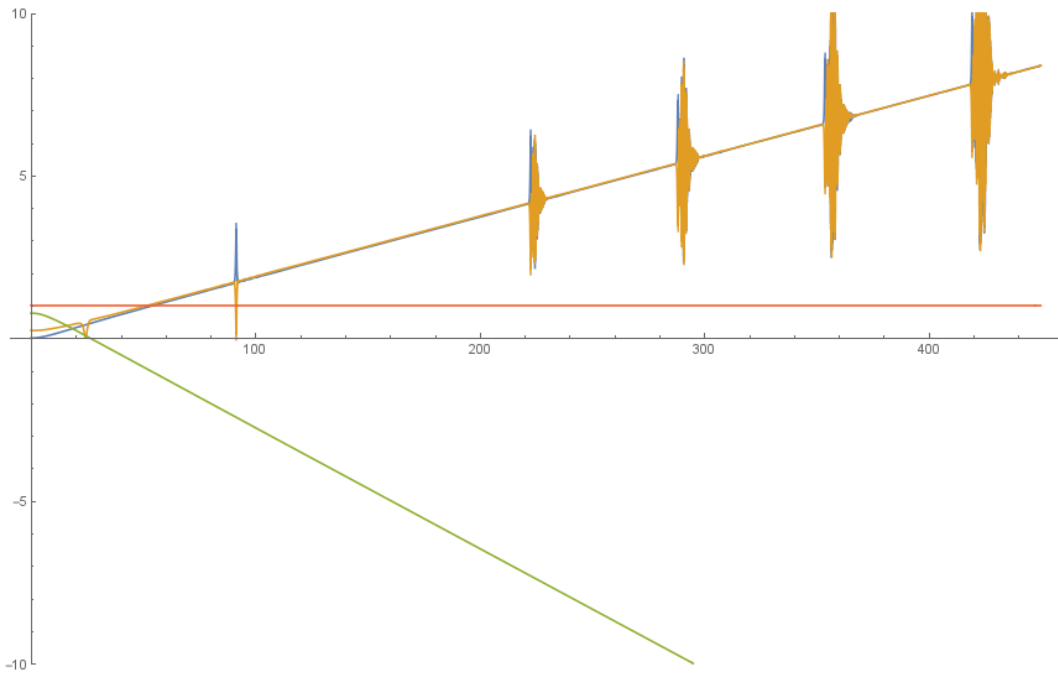


Figure 4.23: Energy distribution in the first example of the sine-Gordon potential. Blue represents kinetic energy, yellow represents the stretch potential energy $\frac{1}{2} \left(\frac{\partial \phi}{\partial x} \right)^2$, and green represents potential energy due to $V(\phi)$, all normalized so that total energy (red) is 1. The x-axis depicts time.

Conclusion

In this dissertation I have explored the connection between quantum theory and cosmology via two projects which link phenomena from each.

Entanglement harvesting links the development of quantum entanglement between two Unruh-DeWitt detectors with the properties of the spacetime in which the detectors are located as encoded in the Wightman function $G_+(x, y)$ of a scalar quantum field on the spacetime. I have extended previous results on entanglement harvesting between accelerating detectors in Minkowski space to analyze the dependence of entanglement harvesting on the dimensionless constant $c_3 = \sigma\Omega$ which characterizes the window function and energy gap of the detectors. This work can be extended by changing the choice of space-time or detector worldlines with the aim of revealing the connection between spacetime geometry and the possibility of entanglement harvesting.

The boom and bust proposal for cosmic inflation links the rapid expansion of the early universe to the dynamics of the inflaton field ϕ whose energy drives inflation. The proposal requires that the inflaton field ϕ nucleate a bubble within a false vacuum via quantum tunneling. I have shown that the lower bound on the size of the compact

extra dimension can be lowered for special choices of potential energy $V(\phi)$ in which the first bubble wall self-collision (and possibly some of the following ones as well) leads to coherent formation of a new vacuum region without significant emission of radiation. One possible extension of this project is to better account for the effect of Hubble friction in the evolution of the bubble in slowing the bubble's expansion, which should also lower the size of the compact extra dimension required for the viability of boom and bust inflation.

Bibliography

1. Einstein, A., Podolsky, B. & Rosen, N. Can quantum-mechanical description of physical reality be considered complete? *Physical review* **47**, 777 (1935).
2. Bell, J. On the Einstein Podolsky Rosen paradox. *Physics* **1** (3 1964).
3. Planck Collaboration. Planck 2015 results-XIII. Cosmological parameters. *Astronomy & Astrophysics* **594**, A13 (2016).
4. Guth, A. H. Inflationary universe: A possible solution to the horizon and flatness problems. *Physical Review D* **23**, 347 (1981).
5. Linde, A. D. A New Inflationary Universe Scenario: A Possible Solution of the Horizon, Flatness, Homogeneity, Isotropy and Primordial Monopole Problems. *Phys. Lett.* **B108**, 389–393 (1982).
6. Brown, A. R. Boom and bust inflation: a graceful exit via compact extra dimensions. *Physical review letters* **101**, 221302 (2008).
7. Holevo, A. S. Bounds for the quantity of information transmitted by a quantum communication channel. *Problemy Peredachi Informatsii* **9**, 3–11 (1973).
8. Wootters, W. K. & Zurek, W. H. A single quantum cannot be cloned. *Nature* **299**, 802–803 (1982).
9. Dieks, D. Communication by EPR devices. *Physics Letters A* **92**, 271–272 (1982).
10. Shor, P. W. Polynomial-time algorithms for prime factorization and discrete logarithms on a quantum computer. *SIAM review* **41**, 303–332 (1999).
11. Amico, L., Fazio, R., Osterloh, A. & Vedral, V. Entanglement in many-body systems. *Reviews of Modern Physics* **80**, 517 (2008).
12. Peres, A. Separability criterion for density matrices. *Physical Review Letters* **77**, 1413 (1996).

13. Horodecki, M., Horodecki, P. & Horodecki, R. Separability of mixed states: necessary and sufficient conditions. *Physics Letters A* **223**, 1–8 (1996).
14. Birrell, N. & Davies, P. *Quantum Fields in Curved Space* ISBN: 9780521278584 (Cambridge University Press, 1984).
15. Martín-Martínez, E., Brown, E. G., Donnelly, W. & Kempf, A. Sustainable entanglement production from a quantum field. *Physical Review A* **88**, 052310 (2013).
16. Reznik, B. Entanglement from the vacuum. *Foundations of Physics* **33**, 167–176 (2003).
17. Ver Steeg, G. & Menicucci, N. C. Entangling power of an expanding universe. *Physical Review D* **79**, 044027 (2009).
18. Martín-Martínez, E. & Menicucci, N. C. Cosmological quantum entanglement. *Classical and Quantum Gravity* **29**, 224003 (2012).
19. Nambu, Y. Entanglement Structure in Expanding Universes. *Entropy* **15**, 1847–1874 (2013).
20. Nambu, Y. Entanglement of quantum fluctuations in the inflationary universe. *Physical Review D* **78**, 044023 (2008).
21. Pozas-Kerstjens, A., Louko, J. & Martín-Martínez, E. Degenerate detectors are unable to harvest spacelike entanglement. *arXiv preprint arXiv:1703.02982* (2017).
22. Martín-Martínez, E. & Menicucci, N. C. Entanglement in curved spacetimes and cosmology. *Classical and Quantum Gravity* **31**, 214001 (2014).
23. Pozas-Kerstjens, A. & Martín-Martínez, E. Entanglement harvesting from the electromagnetic vacuum with hydrogenlike atoms. *Physical Review D* **94**, 064074 (2016).
24. Ng, K. K., Mann, R. B. & Martín-Martínez, E. Equivalence principle and QFT: Can a particle detector tell if we live inside a hollow shell? *Physical Review D* **94**, 104041 (2016).
25. Reznik, B., Retzker, A. & Silman, J. Violating Bell’s inequalities in vacuum. *Physical Review A* **71**, 042104 (2005).
26. Osborne, T. J. & Nielsen, M. A. Entanglement in a simple quantum phase transition. *Physical Review A* **66**, 032110 (2002).

27. Osterloh, A., Amico, L., Falci, G. & Fazio, R. Scaling of entanglement close to a quantum phase transition. *Nature* **416**, 608–610 (2002).
28. Vidal, G., Latorre, J. I., Rico, E. & Kitaev, A. Entanglement in quantum critical phenomena. *Physical review letters* **90**, 227902 (2003).
29. Press, W. H., Teukolsky, S. A., Vetterling, W. T. & Flannery, B. P. *Numerical Recipes 3rd Edition: The Art of Scientific Computing* 3rd ed. ISBN: 0521880688, 9780521880688 (Cambridge University Press, New York, NY, USA, 2007).
30. Kahaner, D., Moler, C. & Nash, S. Numerical methods and software. *Englewood Cliffs: Prentice Hall, 1989* **1** (1989).
31. *NIntegrate Integration Strategies* <https://reference.wolfram.com/language/tutorial/NIntegrateIntegrationStrategies.html>. Wolfram Mathematica online documentation. Accessed: 2017-05-18.
32. Salton, G., Mann, R. B. & Menicucci, N. C. Acceleration-assisted entanglement harvesting and rangefinding. *New J. Phys.* **17**, 035001 (2015).
33. Reznik, B., Retzker, A. & Silman, J. Violating Bell’s inequalities in vacuum. *Physical Review A* **71**, 042104 (2005).
34. Coles, P. & Lucchin, F. *Cosmology: The Origin and Evolution of Cosmic Structure* ISBN: 9780470852996 (Wiley, 2003).
35. Misner, C. W. Mixmaster universe. *Physical Review Letters* **22**, 1071 (1969).
36. Lahav, O. & Liddle, A. R. The cosmological parameters 2006. *arXiv preprint astro-ph/0601168* (2006).
37. Guth, A. H. & Weinberg, E. J. Could the universe have recovered from a slow first-order phase transition? *Nuclear Physics B* **212**, 321–364 (1983).
38. Albrecht, A. & Steinhardt, P. J. Cosmology for grand unified theories with radiatively induced symmetry breaking. *Physical Review Letters* **48**, 1220 (1982).
39. Linde, A. Eternally existing selfreproducing chaotic inflationary universe, 1986. *Phys. Lett. B* **175**, 604.
40. Coleman, S. Fate of the false vacuum: Semiclassical theory. *Physical Review D* **15**, 2929 (1977).
41. Callan Jr, C. G. & Coleman, S. Fate of the false vacuum. II. First quantum corrections. *Physical Review D* **16**, 1762 (1977).

42. Coleman, S. & De Luccia, F. Gravitational effects on and of vacuum decay. *Physical Review D* **21**, 3305 (1980).
43. Coleman, S. in *The whys of subnuclear physics* 805–941 (Springer, 1979).
44. Watkins, R. & Widrow, L. M. Aspects of reheating in first-order inflation. *Nuclear Physics B* **374**, 446–468 (1992).
45. Giblin Jr, J. T., Hui, L., Lim, E. A. & Yang, I.-S. How to run through walls: dynamics of bubble and soliton collisions. *Physical Review D* **82**, 045019 (2010).
46. Amin, M. A., Lim, E. A. & Yang, I.-S. A scattering theory of ultrarelativistic solitons. *Physical Review D* **88**, 105024 (2013).
47. Easter, R., Giblin Jr, J. T., Hui, L. & Lim, E. A. New mechanism for bubble nucleation: Classical transitions. *Physical Review D* **80**, 123519 (2009).
48. Ahlqvist, P., Eckerle, K. & Greene, B. Bubble universe dynamics after free passage. *arXiv preprint arXiv:1310.6069* (2013).
49. Appelquist, T., Chodos, A. & Freund, P. *Modern Kaluza-Klein theories* ISBN: 9780201098297 (Addison-Wesley Pub. Co., 1987).
50. Arkani-Hamed, N., Dimopoulos, S. & Dvali, G. The hierarchy problem and new dimensions at a millimeter. *Physics Letters B* **429**, 263–272 (1998).
51. Kapner, D. *et al.* Tests of the gravitational inverse-square law below the dark-energy length scale. *Physical Review Letters* **98**, 021101 (2007).
52. Sanz-Serna, J. M. & Calvo, M. *Numerical Hamiltonian problems* ISBN: 9780412542909 (Chapman & Hall, 1994).
53. Benettin, G. & Giorgilli, A. On the Hamiltonian interpolation of near-to-the identity symplectic mappings with application to symplectic integration algorithms. *Journal of Statistical Physics* **74**, 1117–1143 (1994).
54. Hairer, E. & Lubich, C. The life-span of backward error analysis for numerical integrators. *Numerische Mathematik* **76**, 441–462 (1997).
55. Reich, S. Backward error analysis for numerical integrators. *SIAM Journal on Numerical Analysis* **36**, 1549–1570 (1999).
56. Weinberg, E. J. *Classical solutions in quantum field theory: Solitons and Instantons in High Energy Physics* (Cambridge University Press, 2012).

57. Makhankov, V. G. *Soliton phenomenology* (Springer Science & Business Media, 2012).
58. Gani, V. A., Kudryavtsev, A. E. & Lizunova, M. A. Kink interactions in the (1+1)-dimensional ϕ^6 model. *Phys. Rev.* **D89**. [Phys. Rev.D89,125009(2014)], 125009 (2014).